

1

1

2 Laminar-specific cortical dynamics in human visual and sensorimotor cortices

3

4 **James J Bonaiuto¹, Sofie S Meyer^{1,2}, Simon Little³, Holly Rossiter⁴, Martina F Callaghan¹, Fred Dick⁵,**
5 **Gareth R Barnes^{1*}, Sven Bestmann^{1,3*}**

6 *: joint last author

7

8 1) Wellcome Centre for Human Neuroimaging, UCL Institute of Neurology, University College
9 London, 12 Queen Square, London, UK

10 2) UCL Institute of Cognitive Neuroscience, University College London, 17 Queen Square, London, UK

11 3) Sobell Department of Motor Neuroscience and Movement Disorders, UCL Institute of Neurology,
12 University College London, 33 Queen Square, London, UK

13 4) CUBRIC, School of Psychology, Cardiff University, Cardiff, UK

14 5) Birkbeck College, University of London, London, UK

15

16 **Corresponding author and Lead contact:** j.bonaiuto@ucl.ac.uk; @jbonaiuto

17

18 **Abstract**

19 Lower frequency, feedback, activity in the alpha and beta range is thought to predominantly
20 originate from infragranular cortical layers, whereas feedforward signals in the gamma range stem
21 largely from supragranular layers. Distinct anatomical and spectral channels may therefore play
22 specialized roles in communication within hierarchical cortical networks; however, empirical
23 evidence for this organization in humans is limited. We leverage high precision MEG to test this
24 proposal, directly and non-invasively, in human participants during visually guided actions. Visual
25 alpha activity mapped onto deep cortical laminae, whereas visual gamma activity predominantly
26 arose from superficial laminae. This laminar-specificity was echoed in sensorimotor beta and gamma
27 activity. Visual gamma activity scaled with task demands in a way compatible with feedforward
28 signaling. For sensorimotor activity, we observed a more complex relationship with feedback and
29 feedforward processes. Distinct frequency channels thus operate in a laminar-specific manner, but
30 with dissociable functional roles across sensory and motor cortices.

31

32 **Keywords**

33 MEG, cortical laminae, action selection, feedback, feedforward

34

35

36 **Introduction**

37 The cerebral cortex is hierarchically organized via feedback connections that originate
38 predominantly from deep layers, and feedforward connections that predominate in superficial layers
39 (Barone et al., 2000; Felleman and Van Essen, 1991; Markov et al., 2013, 2014a, 2014b). Evidence
40 from non-human animal models suggests that information along those pathways is carried via
41 distinct frequency channels: lower frequency (<30Hz) signals predominantly arise from deeper,
42 infragranular layers, whereas higher frequency (>30Hz) rhythms stem largely from more superficial,
43 supragranular layers (Bollimunta et al., 2008, 2011; Buffalo et al., 2011; Haegens et al., 2015; van
44 Kerkoerle et al., 2014; Maier et al., 2010; Roopun et al., 2006, 2010; Smith et al., 2013; Sotero et al.,
45 2015; Spaak et al., 2012; Sun and Dan, 2009; Xing et al., 2012). These data have inspired general
46 theories of cortical functional organization which ascribe specific computational roles to these
47 pathways (Adams et al., 2013; Arnal and Giraud, 2012; Bastos et al., 2012; Donner and Siegel, 2011;
48 Fries, 2005, 2015; Friston and Kiebel, 2009; Jensen and Mazaheri, 2010; Jensen et al., 2015; Stephan
49 et al., 2017; Wang, 2010). In these proposals, lower frequency activity subserves feedback, top-down
50 communication, locked to infragranular layers, whereas high-frequency activity is predominantly
51 carried via feedforward projections from supragranular layers and conveys feedforward, bottom-up
52 information.

53 However, evidence for these proposals in humans is largely indirect and focused on visual and
54 auditory areas (Fontolan et al., 2014; Kok et al., 2016; Koopmans et al., 2010; Michalareas et al.,
55 2016; Olman et al., 2012; Scheeringa and Fries, 2017). Whether one can indeed attribute low and
56 high frequency activity in humans to laminar-specific channels, throughout the cortical hierarchy,
57 remains unclear. Here we leverage recent advances in high precision magnetoencephalography
58 (MEG; Meyer et al., 2017; Troebinger et al., 2014a) to address this issue directly and non-invasively
59 across human visual and sensorimotor cortex.

60 MEG is a direct measure of neural activity (Baillet, 2017), with millisecond temporal precision that
61 allows for delineation of brain activity across distinct frequency bands. Recently developed 3D
62 printed head-cast technology gives us precise models of the underlying cortical anatomy and allows
63 us to record higher SNR MEG data than previously achievable (Meyer et al., 2017; Troebinger et al.,
64 2014a). Theoretical and simulation work shows that these gains allow for distinguishing the MEG
65 signal originating from either deep or superficial laminae (Troebinger et al., 2014b), in a time-
66 resolved and spatially localized manner (Bonaiuto et al., 2017). We therefore employed this
67 approach to directly test for the proposed laminar-specificity of distinct frequency channels in
68 human cortex. Such a demonstration would provide important clarification for the proposed
69 mechanism of inter-regional communication in hierarchical cortical networks.

70

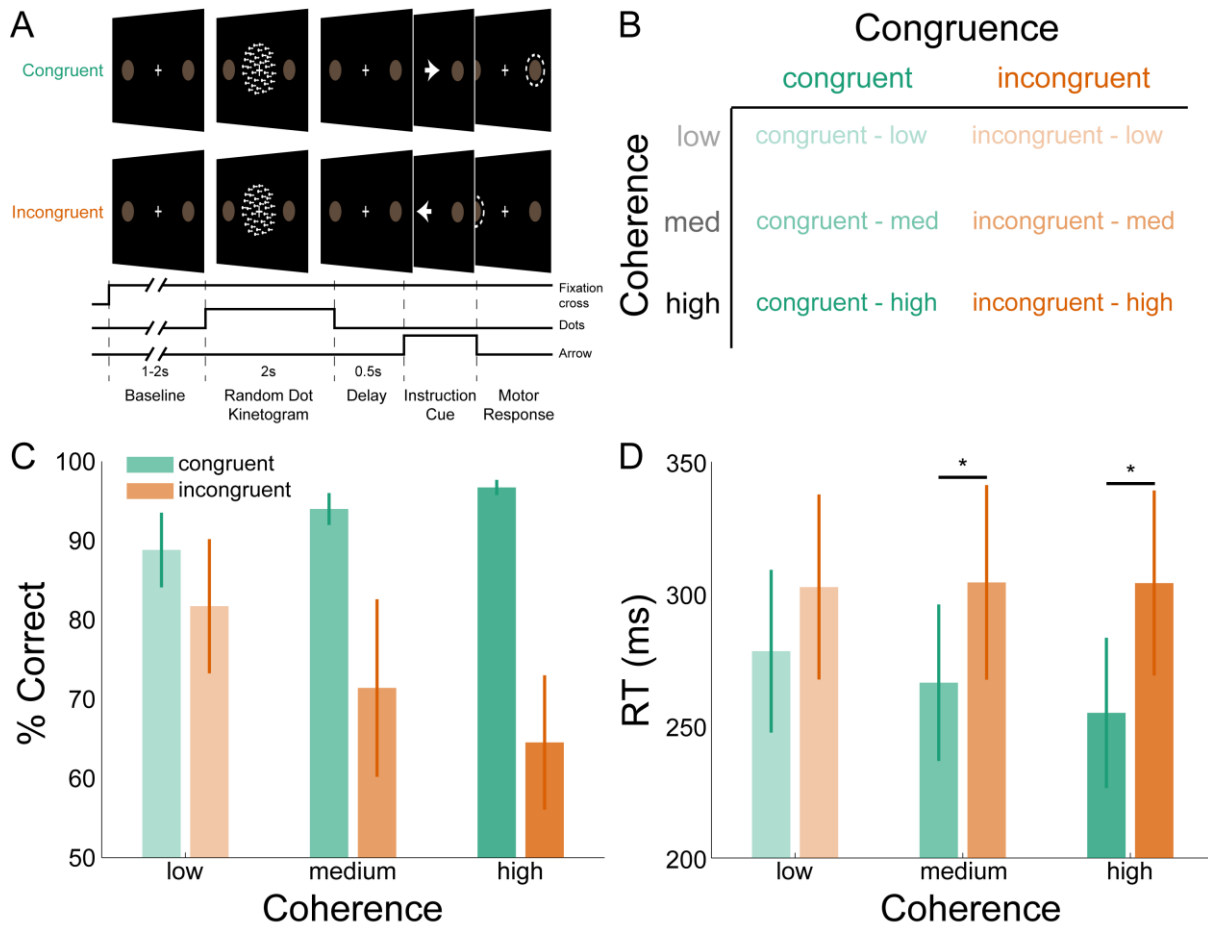
71 **Results**

72

73 **Behavioral responses vary with perceptual evidence and cue congruence**

74 We investigated the laminar and spectral specificity of feedforward and feedback signals in visual
75 and sensorimotor cortex with a visually guided action selection task. The task was designed to
76 induce well-studied patterns of low- and high-frequency activity in visual (Busch et al., 2004; Fries et
77 al., 2001; Hari and Salmelin, 1997; Hoogenboom et al., 2006; Mazaheri et al., 2014; Müller et al.,
78 1996; Muthukumaraswamy and Singh, 2013; Sauseng et al., 2005; Thut, 2006; Yamagishi et al., 2005)
79 and sensorimotor cortices (Cheyne et al., 2008; Crone et al., 1998; Donner et al., 2009; Gaetz et al.,
80 2011; Haegens et al., 2011; Huo et al., 2010; de Lange et al., 2013; Pfurtscheller and Neuper, 1997;
81 Pfurtscheller et al., 1996; Tan et al., 2016, 2014; Torrecillos et al., 2015). Participants first viewed a
82 random dot kinetogram (RDK) with coherent motion to the left or the right, which in most trials was
83 congruent to the direction of the following instruction cue indicating the required motor response
84 (**Figure 1A**). Participants could therefore accumulate the sensory evidence from the RDK in order to

85 prepare their response in advance of the instruction cue, but in incongruent trials the instruction cue
 86 indicated that a different response was required. The strength of the motion coherence was varied,
 87 modulating the strength of feedforward and feedback activity (**Figure 1B**; Donner et al., 2009; de
 88 Lange et al., 2013).
 89



90 **Figure 1. Task structure and participant behavior.** A) Each trial consisted of a fixation baseline (1-2s), random dot
 91 kinetogram (RDK; 2s), delay (0.5s), and instruction cue intervals, followed by a motor response (left/right button press) in
 92 response to the instruction cue. During congruent trials the coherent motion of the RDK was in the same direction that the
 93 arrow pointed in the instruction cue, while in incongruent trials the instruction cue pointed in the opposite direction. B) The
 94 task involved a factorial design, with three levels of motion coherence in the RDK and congruent or incongruent instruction
 95 cues. Most of the trials (70%) were congruent. C) Mean accuracy over participants during each condition. Error bars denote
 96 the standard error. Accuracy increased with increasing coherence in congruent trials, and worsened with increasing
 97 coherence in incongruent trials. D) The mean response time (RT) decreased with increasing coherence in congruent trials
 98 and slowed with increasing coherence in incongruent trials (* $p < 0.05$).
 99

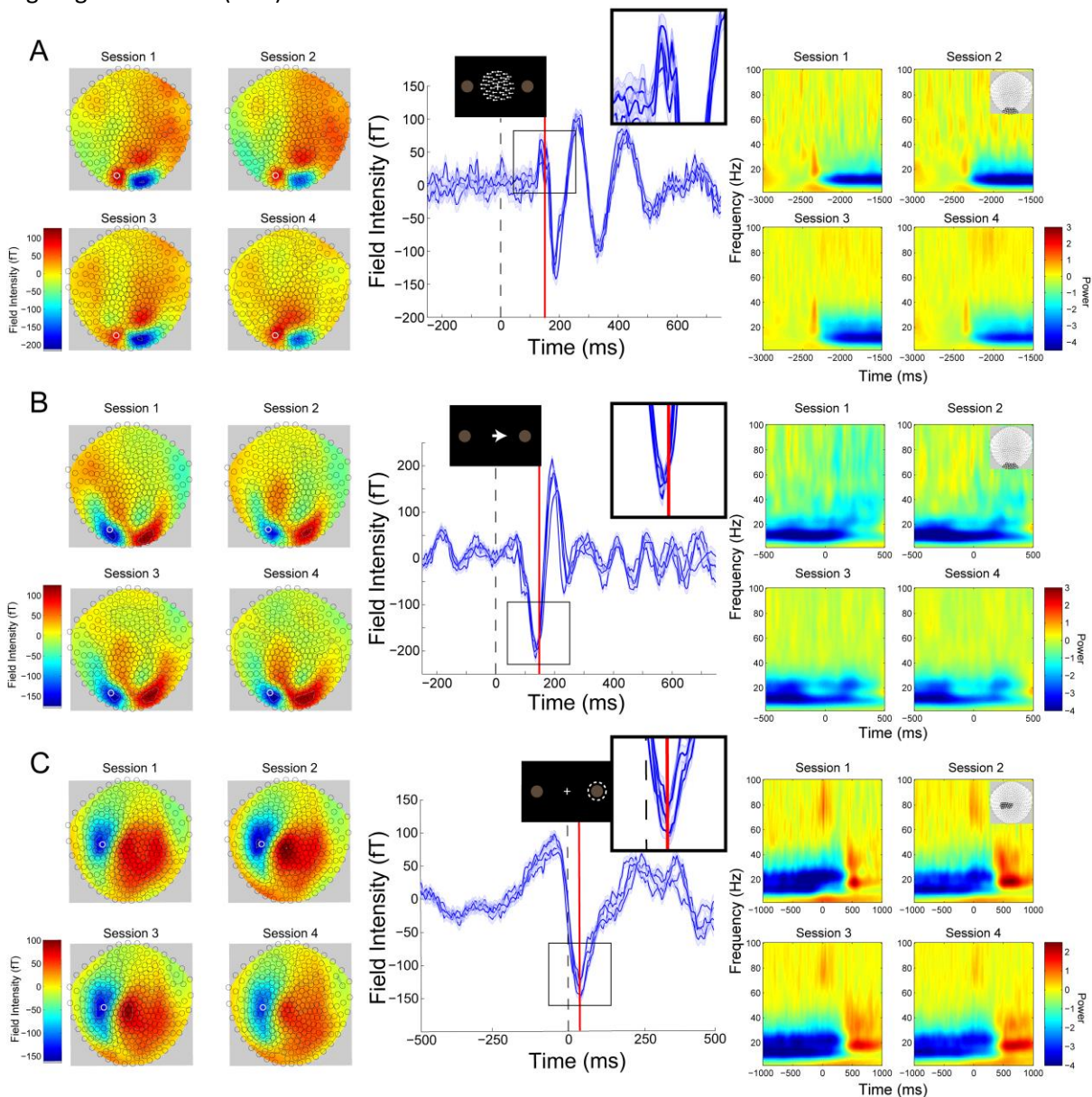
100

101 As expected, participants responded more accurately and more quickly with increasing RDK motion
 102 coherence during congruent trials, while behavioral performance worsened with increasing
 103 coherence during incongruent trials (**Figure 1C, D**). This was demonstrated by a significant
 104 interaction between congruence and coherence for accuracy ($F(2,35)=8.201, p=0.004$), and RT
 105 ($F(2,35)=7.392, p=0.006$). Pairwise comparisons (Bonferroni corrected) showed that RTs were faster
 106 during congruent trials than incongruent trials at medium ($t(7)=-3.235, p=0.0429$) and high
 107 coherence levels ($t(7)=-3.365, p=0.036$). Participants were thus faster and more accurate when the
 108 cued action matched the action they had prepared (congruent trials), and slower and less accurate
 109 when these actions were incongruent.

110

111 **High SNR MEG recordings through individualized headcasts**

112 Subject-specific headcasts minimize both within-session movement and co-registration error (Meyer
113 et al., 2017; Troebinger et al., 2014a). This ensures that when MEG data are recorded over separate
114 days, MEG sensors remain in the same location with respect to the brain. In all participants, within-
115 session movement was less than 0.2mm in the x and y dimensions and less than 1.5mm in the z
116 dimension, and co-registration error was less than 1.5mm in any dimension (**Figure S1**). To assess
117 the between-session homogeneity of our data, we examined topographic maps, event-related fields
118 (ERFs), and time-frequency decompositions aligned to the onset of the RDK (**Figure 2A**), instruction
119 cue (**Figure 2B**), and button response (**Figure 2C**) across recording sessions, which were spaced at
120 least a week apart. This revealed that topographic maps and event-related fields from individual
121 MEG sensors and time-frequency spectra from sensor clusters are highly repeatable and conserved
122 across different days of recording within an individual. Because the headcast approach ensured that
123 participants were in an identical position on repeated days of recording, we were able to obtain very
124 high signal-to-noise (SNR) datasets.



125 **Figure 2: Reproducibility.** Topographic maps (left), event-related fields (ERFs, middle), and time-frequency decompositions
126 (right) aligned to: A) the random dot kinetogram (RDK), B) instruction cue, and C) participant response for a sample
127 participant for four sessions on different days (each including three, 15 minute blocks). The white circles on the topographic
128 maps denote the sensor from which the ERFs in the middle are recorded. Each blue line in the ERF plots represents a single
129 session, with shading representing the standard error (within-session variability) and the red lines show the time point that
130 the topographic maps are plotted for (150ms for the RDK and instruction cue, 35ms for the response). The insets show a
131

132 *magnified view of the plot within the black square. The time-frequency decompositions are baseline corrected (RDK-aligned:*
133 *[-500, 0ms]; instruction cue-aligned: [-3s, -2.5s]; response-aligned: [-500ms, 0ms relative to the RDK]) and averaged over*
134 *the sensors shown in the insets.*

135

136

137 **Low and high frequency activity localize to different cortical laminae**

138 To address our main question about the laminar specificity of different frequency channels in human
139 cortex, we extracted task-related low- and high-frequency activity from visual and sensorimotor
140 cortices. Attention to visual stimuli is associated with decreases in alpha (Hari and Salmelin, 1997;
141 Mazaheri et al., 2014; Sauseng et al., 2005; Thut, 2006; Yamagishi et al., 2005) and increases in
142 gamma activity in visual cortex (Busch et al., 2004; Fries et al., 2001; Hoogenboom et al., 2006;
143 Müller et al., 1996; Muthukumaraswamy and Singh, 2013). We therefore examined the decrease in
144 alpha (7-13Hz) power following the onset of the RDK, as well as the increase in gamma (60-90Hz)
145 activity following the onset of the RDK and the instruction cue.

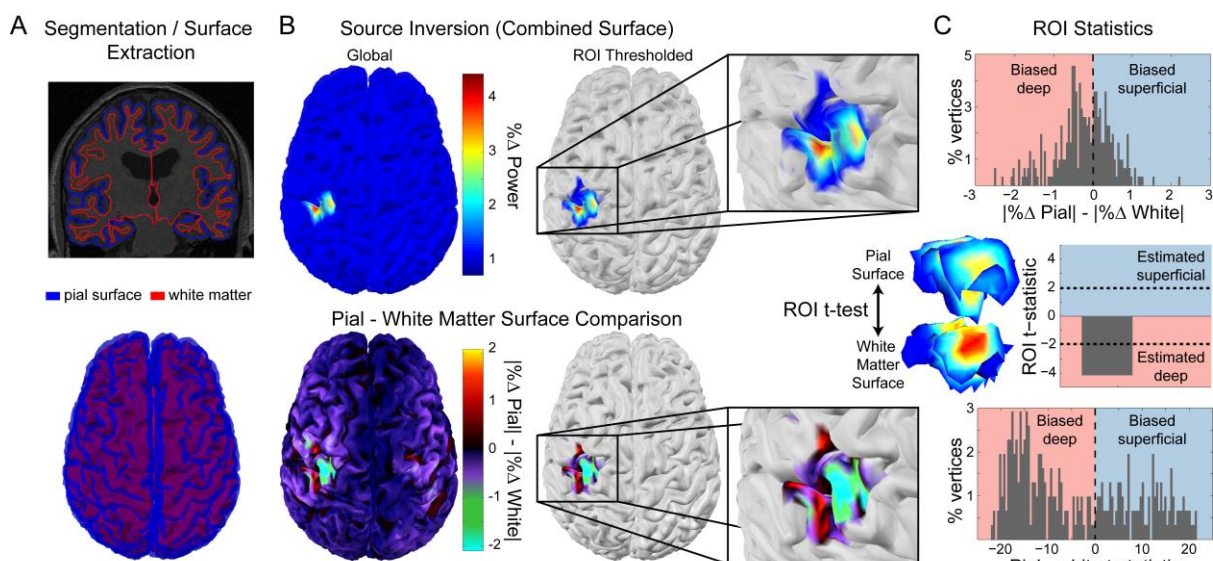
146 Motor responses are associated with a stereotypical pattern of spectral activity in contralateral
147 sensorimotor cortex involving a decrease in beta power during response preparation, followed by a
148 rebound in beta activity. Moreover, a burst of gamma activity typically occurs in contralateral
149 sensorimotor cortex aligned to the movement (Cheyne et al., 2008; Crone et al., 1998; Gaetz et al.,
150 2011; Huo et al., 2010; Pfurtscheller and Neuper, 1997; Pfurtscheller et al., 1996). These two signals
151 are relevant for testing the proposed feedback and feedforward role of low and high frequency
152 activity, respectively, for the following reasons. First, the beta power decrease prior to movement is
153 thought to reflect the removal of inhibition that prevents movement (Engel and Fries, 2010).
154 Moreover, gamma bursts at movement onset arise from motor cortex, are effector-specific, and are
155 thought to reflect the feedback control of discrete movements (Cheyne et al., 2008;
156 Muthukumaraswamy, 2010), and prediction error processing for the purpose of updating motor
157 predictions (Mehrkanoon et al., 2014). The akinetic role of pre-movement beta and the proposed
158 role of movement-related gamma would be difficult to reconcile with the proposed role of these
159 frequency channels in feedback and feedforward control in sensory cortices. This suggests that in
160 sensorimotor cortex, these activity channels may not be organized in the same laminar-specific
161 manner. Alternatively, the same laminar-specific organization may have functional roles that are
162 distinct from the proposed feedback and feedforward communication in sensory cortex. We
163 therefore analyzed the decrease in sensorimotor beta (15-30Hz) power during the RDK and its
164 subsequent rebound following the participant's response, as well as the response-aligned gamma
165 (60-90Hz) burst.

166 Localization of activity measured by MEG sensors requires accurate generative forward models
167 which map from cortical source activity to measured sensor data (Baillet, 2017; Hillebrand and
168 Barnes, 2002, 2003; Larson et al., 2014). We constructed a generative model for each participant
169 based on a surface mesh combining their white matter and pial surfaces, representing both deep
170 and superficial cortical laminae, respectively (**Figure 3**, left column). We are thus able to compare
171 estimated source activity for measured visual and sensorimotor activity on the white matter and pial
172 surface, and infer its laminar origin as deep if the activity is strongest on the white matter surface or
173 superficial if it is strongest on the pial surface. For the purposes of comparison with invasive neural
174 recordings, deep laminae correspond to infragranular cortical layers, and superficial laminae
175 correspond to supragranular layers.

176 The veracity of laminar inferences using this analysis is highly dependent on the accuracy of the
177 white matter and pial surface segmentations. Imprecise surface reconstructions from standard 1mm
178 isotropic T1-weighted volumes result in coarse-grained meshes, which do not accurately capture the
179 separation between the two surfaces, and thus do not allow distinctions to be made between deep
180 and superficial laminae (**Figure S2**). We therefore extracted each surface from high-resolution

181 (800 μ m isotropic) MRI multi-parameter maps (see Methods; **Figure S2**; Carey et al., 2017), allowing
182 fine-grained segmentation of the white matter and pial surfaces.

183 For each low- and high-frequency visual and sensorimotor signal, the laminar analysis compared the
184 absolute change in power from a baseline time window on the vertices of each surface over trials,
185 using paired t-tests. The resulting t-statistic was positive when the change in power was greater on
186 the pial surface (superficial), and negative when the change was greater on the white matter surface
187 (deep; **Figure 3**). To get a global measure of laminar specificity, we averaged the change in power
188 over the whole brain (all vertices) within each surface. In order to make spatially localized laminar
189 inferences, we then defined regions of interest (ROIs) in each subject based on the mean frequency-
190 specific change in power from a baseline time window on vertices from either surface (Bonaiuto et
191 al., 2017; **Figure 3**). We further compared two metrics for defining the ROIs: functionally defined
192 (centered on the vertex with the peak mean difference in power), and anatomically-constrained
193 (centered on the vertex with the peak mean power difference within the visual cortex bilaterally, or
194 in the contralateral motor cortex).
195



196 **Figure 3: Laminar analysis.** Pial and white matter surfaces are extracted from quantitative maps of proton density and T1
197 times obtained from a multi-parameter mapping MRI protocol (A, top). The analysis creates a single generative model
198 combining both surfaces (A, bottom) which is used to perform source inversion using the measured sensor data, resulting in
199 an estimate of the activity at every vertex on each surface (B, top left). The ROI analysis defined a region of interest by
200 comparing the change in power in a particular frequency band during a time window of interest from a baseline time period
201 (B, top right). The ROI included all vertices in either surface in the 80th percentile as well as corresponding vertices in the
202 other surface. The absolute change in power on each surface was then compared within the ROI (B, bottom; C, top).
203 Pairwise t-tests were performed between corresponding vertices on each surface within the ROI to examine the distribution
204 of t-statistics (C, bottom), as well as on the mean absolute change in power within the ROI on each surface to obtain a
205 single t-statistic which was negative if the greatest change in power occurred on the white matter surface, and positive if it
206 occurred on the pial surface (C, middle).
207
208

209 **Visual alpha and gamma have distinct laminar specific profiles**

210 Based on *in vivo* laminar recordings in non-human primates (Bollimunta et al., 2008, 2011; Buffalo et
211 al., 2011; Haegens et al., 2015; van Kerkoerle et al., 2014; Maier et al., 2010; Spaak et al., 2012; Sun
212 and Dan, 2009; Xing et al., 2012), we reasoned that changes in alpha activity following the RDK
213 should predominate in infragranular cortical layers. By contrast, changes in gamma activity following
214 the RDK and instruction cue should be strongest in supragranular layers. Source reconstructions of
215 the change in visual alpha activity following the onset of the RDK on the white matter and pial
216 surfaces approximating the proposed infra- and supragranular origin, are shown for an example
217 participant over the whole brain and within the functionally defined ROI in **Figure 4A**. Activity on
218 both surfaces localized to visual cortex bilaterally. When performing paired t-tests over all trials

219 between corresponding vertices on the pial and white matter surfaces, the distribution of alpha
220 activity was skewed toward the white matter surface, in line with an infragranular origin. This bias
221 was also observed within the functionally defined ROI. When averaging the change in power either
222 over the whole brain, within a functionally-defined, or an anatomically constrained ROI, the visual
223 alpha activity of most participants was classified as originating from the white matter surface (global:
224 8/8 participants, functional ROI: 7/8 participants, anatomical ROI: 5/8 participants; **Figure 4A**, right).

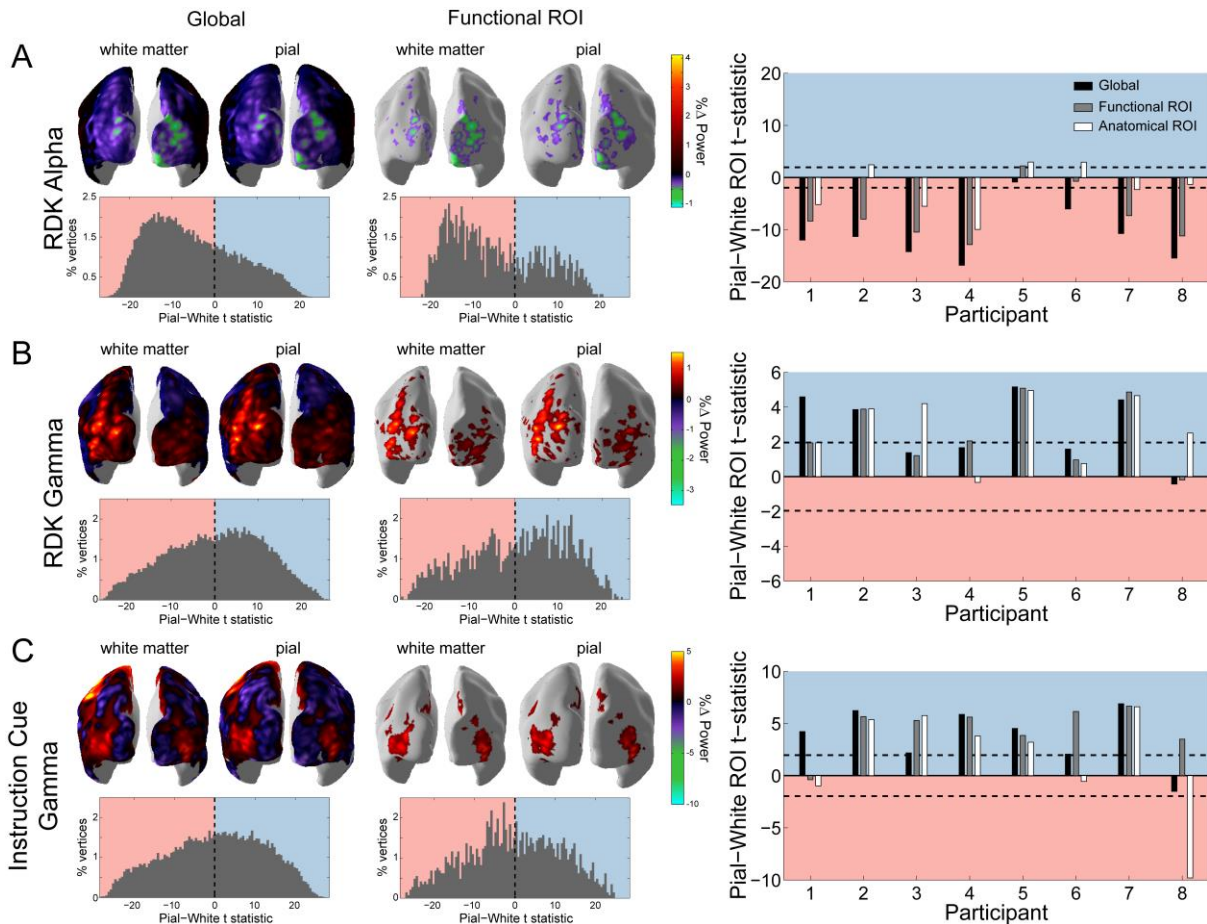
225 Conversely, the increase in visual gamma following the onset of the RDK and instruction cue was
226 strongest on the pial surface (**Figure 4B, C**). Example source reconstructions on the pial and the
227 white matter surface show activity in the same bilateral areas over visual cortex as visual alpha
228 (**Figure 4B, C**). For visual gamma, the distributions of t-statistics for pairwise vertex comparisons
229 were skewed toward the pial surface, a finding that is compatible with a supragranular origin of
230 high-frequency gamma activity. This was confirmed in subsequent global, functional, and anatomical
231 ROI metrics (RDK gamma, global: 7/8 participants; RDK gamma, functional ROI: 7/8 participants; RDK
232 gamma, anatomical ROI: 7/8 participants; instruction cue gamma, global: 7/8 participants;
233 instruction cue gamma, functional ROI: 7/8 participants; instruction cue gamma, anatomical ROI: 5/8
234 participants).

235 We then conducted three control analyses to ascertain the robustness of our findings: shuffling of
236 the position of the sensors, simulation of increased co-registration error, and decreasing effective
237 SNR by using only a random subset of the trials for each participant (see Supplemental Information).
238 Shuffling the position of the sensors destroys any correspondence between the anatomy and the
239 sensor data. Added co-registration error simulates the effect of between-session spatial uncertainty
240 arising from head movement and inaccuracies of the forward model typically experienced without
241 headcasts (Hillebrand and Barnes, 2003, 2011; Medvedovsky et al., 2007; Troebinger et al., 2014b;
242 Uutela et al., 2001). For both control analyses, visual alpha and gamma activity now localized to the
243 pial surface (**Figure S3, S4**), suggesting that the laminar discrimination between visual alpha and
244 gamma in our main analyses would not have been possible were it not for the high-SNR data
245 coupled with the high-precision anatomical models.

246 The magnitude of the ROI t-statistics for all participants increased with the number of trials used in
247 the analysis, with more trials required for visual gamma signals to reach significance (**Figure S5**).
248 Therefore the laminar bias exhibited by visual alpha and gamma was unlikely to be driven by a small
249 subset of the trials. One concern was that the effects could be driven by signal power (i.e. higher
250 power signals always localize deeper). Importantly however, regardless of the SNR the poor
251 anatomical models did not show this behaviour within the functionally defined and anatomically
252 constrained ROIs (**Figure S5**).

253

8



254 **Figure 4: Laminar specificity of visual alpha and gamma.** A) Estimated changes in alpha power (7-13Hz) from baseline on
 255 the white matter and pial surface following the onset of the random dot kinetogram (RDK), over the whole brain and within
 256 a functionally defined region of interest (ROI). Histograms show the distribution of t-statistics comparing the absolute
 257 change in power between pial and white matter surface vertices over the whole brain, or within the ROI.
 258 Negative t-statistics indicate a bias toward the white matter surface, and positive t-statistics indicate a pial bias. The bar
 259 plots show the t-statistics comparing the absolute change in power between the pial and white matter surfaces averaged
 260 within the ROIs, over all participants. T-statistics for the whole brain (black bars), functionally defined (grey bars), and
 261 anatomically constrained (white bars) ROIs are shown (red = biased toward the white matter surface, blue = biased pial).
 262 Dashed lines indicate the threshold for single subject statistical significance. B) As in A, for gamma (60-90Hz) power
 263 following the RDK. C) As in A and B, for gamma (60-90Hz) power following the instruction cue.

265

266

267 **Sensorimotor beta and gamma originate from distinct cortical laminae**

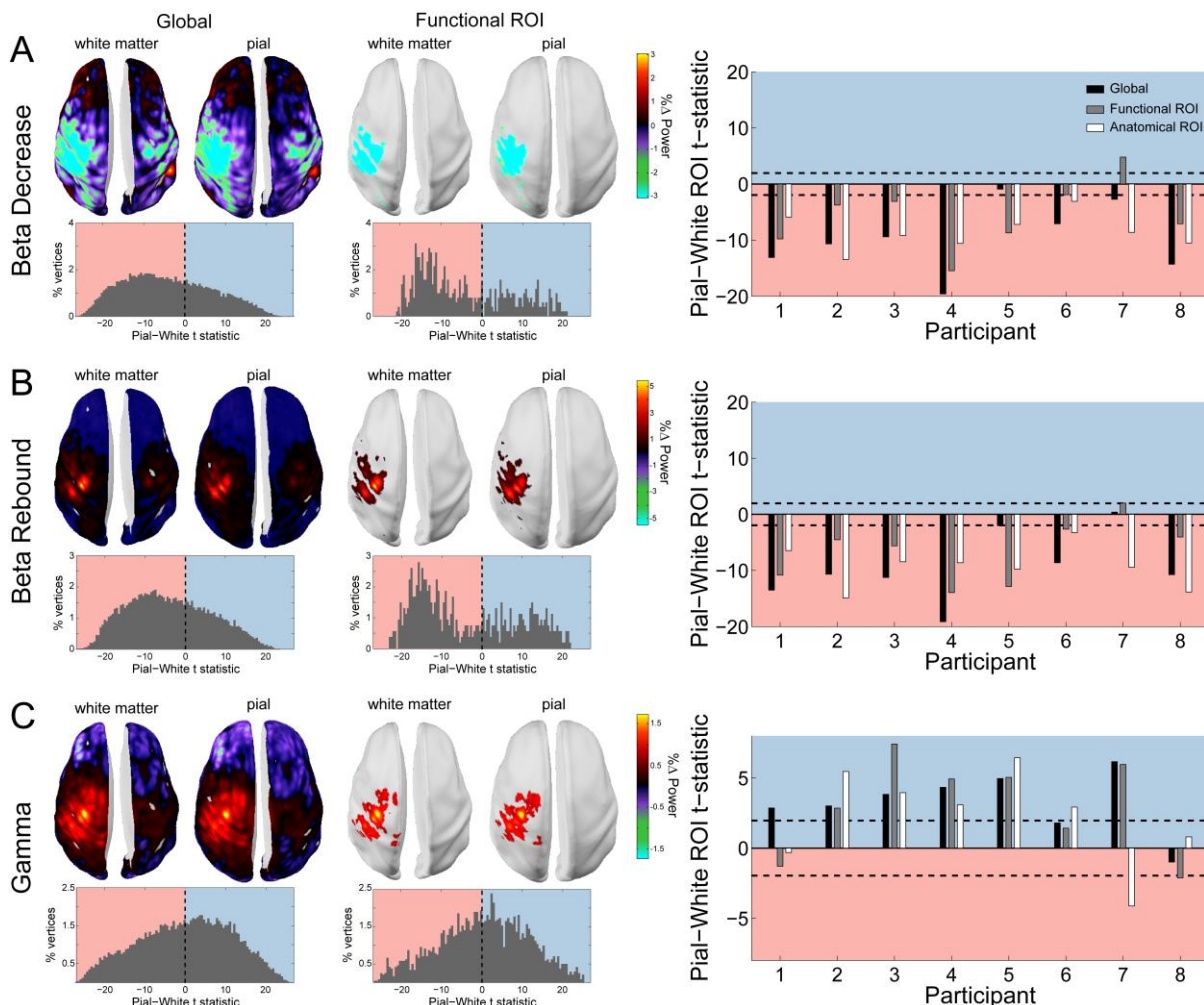
268 The above results provide novel support for distinct anatomical pathways through which different
 269 frequency channels contribute to intra-areal communication. We next addressed whether this
 270 laminar specificity of different frequency channels occurred throughout cortex. Cortical regions vary
 271 in terms of thickness (Fischl and Dale, 2000; Jones et al., 2000; Kabani et al., 2001; Lerch and Evans,
 272 2005; MacDonald et al., 2000), as a result of inter-regional variation in cortical folding and the
 273 morphology of cortical layers (Barbas and Pandya, 1989; Hilgetag and Barbas, 2006; Matelli et al.,
 274 1991; Rajkowska and Goldman-Rakic, 1995). Moreover, the distinction of feedback and feedforward
 275 cortical processing channels may be less clear for motor cortex, which is agranular and projects to
 276 the spinal cord. Supporting this argument, motor gamma bursts are closely tied to movement onset,
 277 and thought to reflect the execution, or feedback control, of movement (Cheyne and Ferrari, 2013;
 278 Cheyne et al., 2008). While frequency-specific activity thus occurs throughout cortex, the laminar
 279 distribution of different frequency channels may differ across different levels in the cortical
 280 hierarchy. Because MEG is only sensitive to the synchronous activity of large populations of

281 pyramidal cells, it is likely that different laminar microcircuits could give rise to the same measurable
282 MEG signals (Cohen, 2017). Alternatively, if the layer specificity of low and high frequency activity is
283 a general organizing principle of cortex, one would expect the pre-movement beta decrease and
284 post-movement rebound to originate from infragranular cortical layers, and the movement-related
285 gamma increase to be strongest in supragranular layers. Moreover, the ability of MEG to accurately
286 segregate deep from superficial laminar source activity may vary throughout cortex, a possibility we
287 have previously explored (Bonaiuto et al., 2017).

288 We analyzed two task-related modulations of sensorimotor beta activity: the decrease in beta power
289 following the onset of the RDK, just prior to the motor response, and the post-movement beta
290 rebound (Cassim et al., 2001; Jurkiewicz et al., 2006; Parkes et al., 2006; Pfurtscheller et al., 1996;
291 Salmelin et al., 1995). Both signals localized to the left sensorimotor cortex (contralateral to the
292 hand used to indicate the response; **Figure 5A, B**), and both signals were strongest on the white
293 matter surface, as evidenced by the white matter skews in the global and functional ROI t-statistics.
294 This laminar pattern held for all but one participant, with both the beta decrease and rebound
295 classified as originating from the white matter surface. This is of relevance as it addresses concerns
296 that the high SNR of beta activity trivially leads to its attribution to the deeper cortical surface. Here,
297 the two epochs of beta activity were characterized by power decreases and increases, respectively.

298 The burst of gamma aligned with the onset of the movement localized to the same patch of left
299 sensorimotor cortex (**Figure 5C**), but in the example participant shown in **Figure 5** and for most
300 participants, was strongest on the pial surface (global: 7/8 participants; function ROI: 6/8
301 participants; anatomical ROI: 6/8 participants).

302



303

304 **Figure 5: Laminar specificity of sensorimotor beta and gamma.** As in figure 5, for A) the beta (15-30Hz) decrease prior to
305 the response, B) beta (15-30Hz) rebound following the response, and C) gamma (60-90Hz) power change from baseline
306 during the response. In the histograms and bar plots, positive and negative values indicate a bias towards the superficial
307 and deeper cortical layers, respectively. The dashed lines indicate single subject level significance thresholds. The black,
308 grey, and white bars indicate statistics based on regions of interest comprising the whole brain, functional and
309 anatomically-constrained ROIs, respectively.

310

311 The results of the sensorimotor laminar control analyses mirrored those of visual alpha and gamma.
312 Sensor shuffling, as well as the addition of co-registration error, resulted in sensorimotor beta and
313 gamma localizing to the pial surface (**Figure S3, S4**), and the ROI t-statistics increased in magnitude
314 with the number of trials used in the analysis, with more trials required for sensorimotor gamma
315 signals to pass the significance threshold (**Figure S5**). Again, importantly, the gamma superficial bias
316 within the functionally defined and anatomically constrained ROIs did not increase with SNR for the
317 poor anatomical models (**Figure S5**).

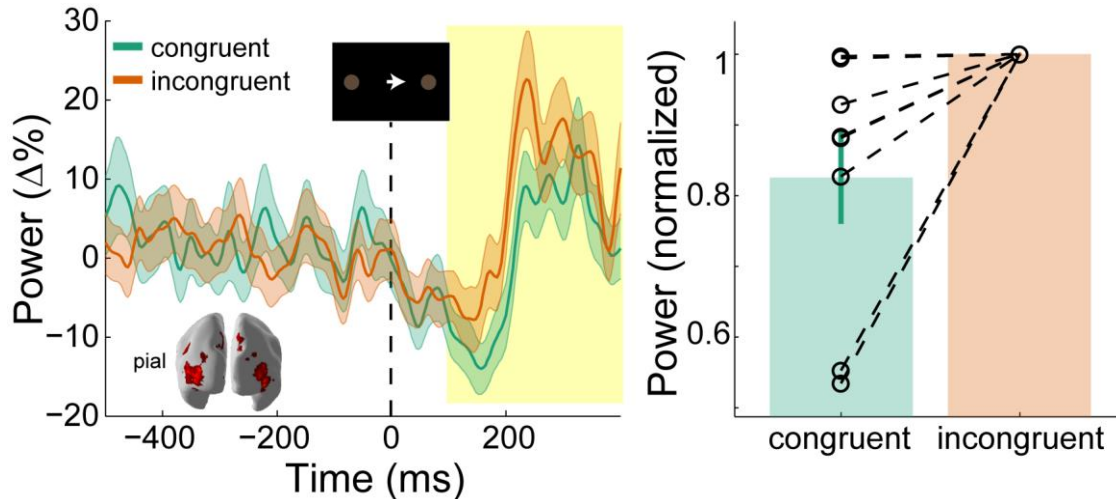
318

319 **Superficial visual gamma scales with cue congruence**

320 Finally, we asked whether the observed low and high-frequency laminar-specific activity in visual and
321 sensorimotor cortex dynamically varied with task demands in line with proposals about their role in
322 feedback and feedforward message passing. This would provide additional indirect support for the
323 idea that communication in hierarchical cortical networks is organized through distinct frequency
324 channels along distinct anatomical pathways, to orchestrate top-down and bottom-up control.

325 In our task, the direction of the instruction cue was congruent to the motion coherence direction in
326 the RDK during most trials. For example, if the direction of motion coherence is to the left, the
327 instruction cue will most likely be a leftward arrow. Gamma activity increases in sensory areas during
328 presentation of unexpected stimuli (Arnal et al., 2011; Gurtubay et al., 2001; Todorovic et al., 2011),
329 and therefore we expected visual gamma activity in supragranular layers to be greater following
330 incongruent instruction cues than after congruent cues. Indeed, the increase in visual gamma on the
331 pial surface following the onset of the instruction cue was greater in incongruent compared to
332 congruent trials ($W(8)=0$, $p=0.008$; 8/8 participants; incongruent-congruent $M=1.64\%$, $SD=2.34\%$;
333 **Figure 6**).

334



335

336

337

338

339

340

341

342

343

Figure 6: Visual gamma activity by task condition. Visual gamma activity following the onset of the instruction stimulus within the functionally defined ROI of an example participant (left), and averaged within the time window represented by the shaded rectangle for all participants (right). Each dashed line on the right shows the normalized values for each participant. The bar height represents the mean normalized change in gamma power, and the error bars denote the standard error. Visual gamma activity is stronger following the onset of the instruction cue when it is incongruent to the direction of coherent motion in the random dot kinetogram (RDK).

Deep sensorimotor beta scales with RDK motion coherence and cue congruence

344

345

346

347

348

349

350

Changes in sensorimotor beta power during response preparation predict forthcoming motor responses (Donner et al., 2009; Haegens et al., 2011; de Lange et al., 2013), whereas the magnitude of sensorimotor beta rebound is attenuated by movement errors (Tan et al., 2014, 2016; Torrecillos et al., 2015). We therefore predicted that, in infragranular layers, the decrease in sensorimotor beta would scale with the motion coherence of the RDK, and the magnitude of the beta rebound would be decreased during incongruent trials when the prepared movement has to be changed in order to make a correct response.

351

352

353

354

355

356

357

358

359

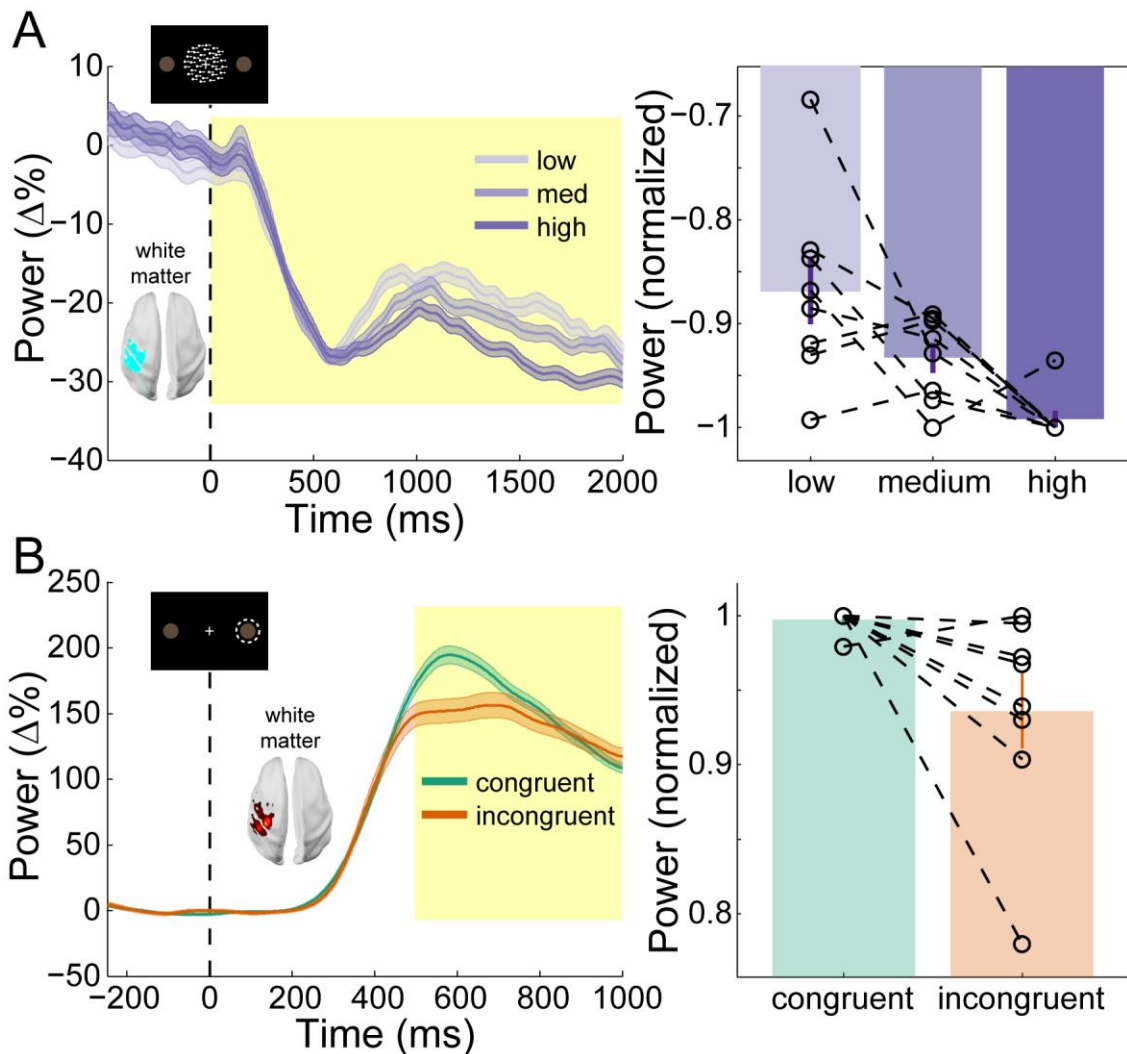
360

361

362

363

The behavioral results suggest that participants accumulated perceptual evidence from the RDK in order to prepare their response prior to the onset of the instruction cue. This preparation was accompanied by a reduction in beta power in the sensorimotor cortex contralateral to the hand used to indicate the response (Figure 5A). This beta decrease began from the onset of the RDK and was more pronounced with increasing coherence, demonstrating a significant effect of coherence on the white matter surface (Figure 7A; $\chi^2(2)=9.75$, $p=0.008$), with beta during high coherence trials significantly lower than during low coherence trials (8/8 participants; $t(7)=-3.496$, $p=0.033$; low-high $M=2.42\%$, $SD=1.96\%$). Following the response, there was an increase in beta in contralateral sensorimotor cortex (beta rebound) which was greater in congruent, compared to incongruent trials on the white matter surface (Figure 7B; $W(8)=34$, $p=0.023$; 7/8 participants, congruent-incongruent $M=5.13\%$, $SD=5.19\%$). In other words, the beta rebound was greatest when the cued response matched the prepared response.



364
365 **Figure 7: Sensorimotor beta activity by task condition.** A) Beta decrease following the onset of the random dot kinetogram
366 (RDK) within the functionally defined ROI of an example participant over the duration of the RDK (left), and averaged over
367 this duration for all participants (right). The bar height represents the mean normalized change in gamma power, and the
368 error bars denote the standard error. The beta decrease becomes more pronounced with increasing coherence. B) As in A,
369 for beta rebound following the response and averaged within the time window shown by the black rectangle. Beta rebound
370 is stronger following responses in congruent trials.

371

372 **Discussion**

373 We have demonstrated that low and high frequency channels localize predominantly to deep and
374 superficial laminae, respectively, in human visual and sensorimotor cortex. These channels play
375 distinct roles in feedback and feedforward processing during visually guided action selection, with
376 high frequency visual activity enhanced by a mismatch between feedforward and feedback signals,
377 and low frequency sensorimotor activity modulated by a combination of feedforward and feedback
378 influences during different task epochs. Through the use of novel MEG head-cast technology (Meyer
379 et al., 2017; Troebinger et al., 2014a) and spatially and temporally resolved laminar analyses
380 (Bonaiuto et al., 2017; Troebinger et al., 2014b), we provide novel evidence for the layer- and
381 frequency-specific accounts of hierarchical cortical organization in humans.

382

383 **Low and high frequency channels localize to deep and superficial cortical laminae across visual and** 384 **sensorimotor cortex**

385 We found that low frequency activity (alpha, 7-13Hz; and beta, 15-30Hz) predominately originated
386 from deep cortical laminae, and high frequency activity (gamma, 60-90Hz) from superficial laminae

387 in both visual and sensorimotor cortex. Our analysis included two built-in controls. Firstly, visually
388 induced gamma after both the RDK and the instruction cue localized superficially, reinforcing the
389 proposal that visual gamma generally predominates from superficial laminae. Secondly, both a
390 decrease and increase in sensorimotor beta power localized to deep laminae, meaning that the
391 laminar analysis was not simply biased toward deep sources for high power signals. Moreover, this
392 laminar specificity was abolished by shuffling the sensors (**Figure S3**) and introducing co-registration
393 error (**Figure S4**), underlining the need for spatially precise anatomical data and MEG recordings.
394 Finally, the laminar bias of both low and high frequency signals increased monotonically as the
395 number of trials included in the analysis increased, but not when the sensors were shuffled (**Figure**
396 **S5**).

397 The localization of alpha activity to predominately deep laminae of visual cortex is in line with
398 evidence from depth electrode recordings in visual areas of the non-human primate brain (Buffalo et
399 al., 2011; van Kerkoerle et al., 2014; Maier et al., 2010; Smith et al., 2013; Spaak et al., 2012; Xing et
400 al., 2012). Several studies who have found alpha generators in both infra- and supragranular layers
401 in primary sensory areas (Bollimunta et al., 2008, 2011; Haegens et al., 2015), and it has been
402 suggested that this discrepancy is due to a contamination of infragranular layer LFP signals by
403 volume conduction from strong alpha generators in supragranular layers (Haegens et al., 2015). This
404 is unlikely to apply to the results presented here as this type of laminar MEG analysis is biased
405 toward superficial laminae when SNR is low (**Figure S3, S4**; Bonaiuto et al., 2017). However, this
406 analysis can only determine the laminar origin of the strongest activity when it occurs
407 simultaneously at multiple depths (Bonaiuto et al., 2017), which is consistent with the fact that
408 infragranular cortical layers contain the primary local pacemaking alpha generators (Bollimunta et
409 al., 2008, 2011).

410 We found that gamma activity was strongest in superficial cortical laminae, which was expected
411 given that gamma activity has been found to predominantly occur in supragranular layers in visual
412 cortex (Buffalo et al., 2011; van Kerkoerle et al., 2014; Smith et al., 2013; Spaak et al., 2012; Xing et
413 al., 2012), but see (Nandy et al., 2017). The mechanisms underlying the generation of gamma activity
414 are diverse across the cortex (Buzsáki and Wang, 2012), but commonly involve reciprocal
415 connections between pyramidal cells and interneurons, or between interneurons (Tiesinga and
416 Sejnowski, 2009; Whittington et al., 2011). The local recurrent connections necessary for such
417 reciprocal interactions are most numerous in supragranular layers (Buzsáki and Wang, 2012), as are
418 fast-spiking interneurons which play a critical role in generating gamma activity (Cardin et al., 2009;
419 Carlén et al., 2012; Sohal et al., 2009).

420 It is widely hypothesized that the laminar segregation of frequency specific channels is a common
421 organizing principle across the cortical hierarchy (Arnal and Giraud, 2012; Bastos et al., 2012; Fries,
422 2015; Wang, 2010). However, most evidence for this claim comes from depth electrode recordings
423 in primary sensory areas, with the vast majority in visual cortical regions (Buffalo et al., 2011; van
424 Kerkoerle et al., 2014; Smith et al., 2013; Spaak et al., 2012; Xing et al., 2012). While *in vivo* laminar
425 data from primate sensorimotor cortex are lacking, *in vitro* recordings from somatosensory and
426 motor cortices demonstrate that beta activity is generated in neural circuits dominated by
427 infragranular layer V pyramidal cells (Roopun et al., 2006, 2010; Yamawaki et al., 2008). By contrast,
428 gamma activity is thought to arise from supragranular layers II/III of mouse somatosensory cortex
429 (Cardin et al., 2009; Carlén et al., 2012). The results presented here support generalized theories of
430 laminar organization across cortex, and are the first to describe the laminar origin of movement-
431 related sensorimotor activity.

432

433 **High frequency activity in visual cortex is enhanced by mismatches in feedforward and feedback**
434 **signals**

435 We found that visual gamma was enhanced following the presentation of the instruction cue in
436 incongruent compared to congruent trials. This was in agreement with our predictions, based on the
437 fact that supragranular layer gamma activity is implicated in feedforward processing (van Kerkoerle
438 et al., 2014). In our task, the direction of coherent motion in the RDK was congruent with the
439 direction of the following instruction cue in most trials. Participants could therefore form a sensory
440 expectation of the direction of the forthcoming instruction cue, which was violated in incongruent
441 trials. The enhancement of visual gamma following incongruent cues is therefore consistent with the
442 gamma activity increase observed in sensory areas during perceptual expectation violations (Arnal et
443 al., 2011; Gurtubay et al., 2001; Todorovic et al., 2011) as well as layer-specific synaptic currents in
444 supragranular cortical layers during performance error processing (Sajad et al., 2017).

445

446 **Low frequency activity in sensorimotor cortex reflects a combination of feedforward and feedback** 447 **processes**

448 There are numerous theories for the computational role of beta activity in motor systems. Decreases
449 in beta power prior to the onset of a movement predict the selected action (Donner et al., 2009;
450 Haegens et al., 2011; de Lange et al., 2013), whereas the beta rebound following a movement is
451 attenuated by error monitoring processes (Tan et al., 2014, 2016; Torrecillos et al., 2015). Our results
452 unify both of these accounts, showing that the level of beta decrease prior to a movement is
453 modulated by the accumulation of sensory evidence predicting the cued movement, while the beta
454 rebound is diminished when the prepared action must be suppressed in order to correctly perform
455 the cued action. This suggests that in the sensorimotor system, low frequency activity can reflect
456 both bottom-up and top-down processes depending on the task epoch. This may occur via bottom-
457 up, feedforward projections from intraparietal regions to motor regions (Hanks et al., 2006; Kayser
458 et al., 2010; Platt and Glimcher, 1999; Tosoni et al., 2008) or top-down, feedback projections from
459 the dorsolateral prefrontal cortex (Curtis and Lee, 2010; Georgiev et al., 2016; Heekeren et al., 2006,
460 2004; Hussar and Pasternak, 2013). The dissociation between bottom-up and top-down influences
461 during different task epochs could indicate that the decrease in beta and the following rebound are
462 the result of functionally distinct processes.

463

464 **Future directions**

465 Our ROI-based comparison of deep and superficial laminae can only determine the origin of the
466 strongest source of activity, which does not imply that activity within a frequency band is exclusively
467 confined to either deep or superficial sources within the same patch of cortex (Bollimunta et al.,
468 2011; Haegens et al., 2015; Maier et al., 2010; Smith et al., 2013; Spaak et al., 2012; Xing et al.,
469 2012). We should also note that in all of our control studies, in which we discard spatial information,
470 a bias towards the superficial (pial) cortical surface was present. However, this bias does not
471 increase with SNR for high frequency activity with poor anatomical models, mirroring the results of
472 simulations showing that this type of laminar analysis is biased superficially at low SNR levels, but
473 that the metrics are not statistically significant at these levels (Bonaiuto et al., 2017). Moreover, we
474 used white matter and pial surface meshes to represent deep and superficial cortical laminae,
475 respectively, and therefore our analysis is insensitive to granular sources. Recent studies have shown
476 that beta, and perhaps gamma, activity is generated by stereotyped patterns of proximal and distal
477 inputs to infragranular and supragranular pyramidal cells (Jones, 2016; Lee and Jones, 2013;
478 Sherman et al., 2016). Future extensions to our laminar analysis could use a sliding time window in
479 order determine the time course of laminar activity. MEG is a global measure of neural activity, and
480 therefore uniquely situated to test large scale computational models of laminar and frequency-
481 specific interactions (Lee et al., 2013; Mejias et al., 2016; Pinotsis et al., 2017; Wang et al., 2013), as
482 well as the possibility that other cortical areas are organized along different principles; for example,
483 in inferior temporal cortex the primary local pacemaking alpha generators are in supragranular
484 layers (Bollimunta et al., 2008). Finally, in the task used here, participants were told that the
485 direction of coherent motion in the RDK predicts the forthcoming instruction cue. Further research

486 will determine how predictive cues are learned implicitly, and how this process shapes beta and
487 gamma activity in visual and sensorimotor areas.

488

489 **Experimental Procedures**

490 **Behavioral Task**

491 Eight neurologically healthy volunteers participated in the experiment (6 male, aged 28.5 ± 8.52
492 years). The study protocol was in full accordance with the Declaration of Helsinki, and all participants
493 gave written informed consent after being fully informed about the purpose of the study. The study
494 protocol, participant information, and form of consent, were approved by the local ethics committee
495 (reference number 5833/001). Participants completed a visually guided action decision making task
496 in which they responded to visual stimuli projected on a screen by pressing one of two buttons on a
497 button box using the index and middle finger of their right hand. On each trial, participants were
498 required to fixate on a small white cross in the center of a screen. After a baseline period randomly
499 varied between 1s and 2s, a random dot kinetogram (RDK) was displayed for 2s with coherent
500 motion either to the left or to the right (**Figure 1A**). Following a 500ms delay, an instruction cue
501 appeared, consisting of an arrow pointing either to the left or the right, and participants were
502 instructed to press the corresponding button (left or right) as quickly and as accurately as possible.
503 Trials ended once a response had been made or after a maximum of 1s if no response was made.

504 The task had a factorial design with congruence (whether or not the direction of the instruction cue
505 matched that of the coherent motion in the RDK) and coherence (the percentage of coherently
506 moving dots in the RDK) as factors (**Figure 1B**). Participants were instructed that in most of the trials
507 (70%), the direction of coherent motion in the RDK was congruent to the direction of the instruction
508 cue. Participants could therefore reduce their mean response time (RT) by preparing to press the
509 button corresponding to the direction of the coherent motion. The RDK consisted of a $10^\circ \times 10^\circ$
510 square aperture centered on the fixation point with 100, 0.3° diameter dots, each moving at $4^\circ/s$.
511 The levels were individually set for each participant by using an adaptive staircase procedure
512 (QUEST; Watson and Pelli, 1983) to determine the motion coherence at which they achieved 82%
513 accuracy in a block of 40 trials at the beginning of each session, in which they had to simply respond
514 with the left or right button to leftwards or rightwards motion coherence. The resulting level of
515 coherence was then used as medium, and 50% and 150% of it as low and high, respectively.

516 Each block contained 126 congruent trials, and 54 incongruent trials, and 60 trials for each
517 coherence level with half containing coherent leftward motion, and half rightward (180 trials total).
518 All trials were randomly ordered. Participants completed 3 blocks per session, and 1-5 sessions on
519 different days, resulting in 540-2700 trials per participant ($M=1822.5$, $SD=813.21$). The behavioral
520 task was implemented in MATLAB (The MathWorks, Inc., Natick, MA) using the Cogent 2000 toolbox
521 (<http://www.vislab.ucl.ac.uk/cogent.php>).

522

523 **MRI Acquisition**

524 Prior to MEG sessions, participants underwent two of MRI scanning protocols during the same visit:
525 one for the scan required to generate the scalp image for the headcast, and a second for MEG
526 source localization. Structural MRI data were acquired using a 3T Magnetom TIM Trio MRI scanner
527 (Siemens Healthcare, Erlangen, Germany). During the scan, the participant lay in the supine position
528 with their head inside a 12-channel coil. Acquisition time was 3 min 42 s, plus a 45 s localizer
529 sequence.

530 The first protocol was used to generate an accurate image of the scalp for headcast construction
531 (Meyer et al., 2017). This used a T1-weighted 3D spoiled fast low angle shot (FLASH) sequence with
532 the following acquisition parameters: 1mm isotropic image resolution, field-of view set to 256, 256,
533 and 192 mm along the phase (anterior-posterior, A-P), read (head-foot, H-F), and partition (right-
534 left, R-L) directions, respectively. The repetition time was 7.96ms and the excitation flip angle was

535 12°. After each excitation, a single echo was acquired to yield a single anatomical image. A high
536 readout bandwidth (425Hz/pixel) was used to preserve brain morphology and no significant
537 geometric distortions were observed in the images. Acquisition time was 3 min 42s, a sufficiently
538 short time to minimize sensitivity to head motion and any resultant distortion. Care was also taken
539 to prevent distortions in the image due to skin displacement on the face, head, or neck, as any such
540 errors could compromise the fit of the headcast. Accordingly, a more spacious 12 channel head coil
541 was used for signal reception without using either padding or headphones.

542 The second protocol was a quantitative multiple parameter mapping (MPM) protocol, consisting of 3
543 differentially-weighted, RF and gradient spoiled, multi-echo 3D FLASH acquisitions acquired with
544 whole-brain coverage at 800 μ m isotropic resolution. Additional calibration data were also acquired
545 as part of this protocol to correct for inhomogeneities in the RF transmit field (Callaghan et al., 2015;
546 Lutti et al., 2010, 2012). For this protocol, data were acquired with a 32-channel head coil to
547 increase SNR.

548 The FLASH acquisitions had predominantly proton density (PD), T1 or magnetization transfer (MT)
549 weighting. The flip angle was 6° for the PD- and MT-weighted volumes and 21° for the T1 weighted
550 acquisition. MT-weighting was achieved through the application of a Gaussian RF pulse 2 kHz off
551 resonance with 4 ms duration and a nominal flip angle of 220° prior to each excitation. The field of
552 view was set to 224, 256, and 179 mm along the phase (A–P), read (H–F), and partition (R–L)
553 directions, respectively. Gradient echoes were acquired with alternating readout gradient polarity at
554 eight equidistant echo times ranging from 2.34 to 18.44 ms in steps of 2.30 ms using a readout
555 bandwidth of 488 Hz/pixel. Only six echoes were acquired for the MT-weighted acquisition in order
556 to maintain a repetition time (TR) of 25 ms for all FLASH volumes. To accelerate the data acquisition
557 and maintain a feasible scan time, partially parallel imaging using the GRAPPA algorithm (Griswold et
558 al., 2002) was employed with a speed-up factor of 2 and forty integrated reference lines in each
559 phase-encoded direction (A–P and R–L).

560 To maximize the accuracy of the measurements, inhomogeneity in the transmit field was mapped by
561 acquiring spin echoes and stimulated echoes across a range of nominal flip angles following the
562 approach described in Lutti et al. (2010), including correcting for geometric distortions of the EPI
563 data due to B0 field inhomogeneity. Total acquisition time for all MRI scans was less than 30 min.

564 Quantitative maps of proton density (PD), longitudinal relaxation rate ($R1 = 1/T1$), magnetization
565 transfer saturation (MT) and effective transverse relaxation rate ($R2^* = 1/T2^*$) were subsequently
566 calculated according to the procedure described in Weiskopf et al. (2013). Each quantitative map
567 was co-registered to the scan used to design the headcast, using the T1 weighted map. The resulting
568 maps were used to extract cortical surface meshes using FreeSurfer (see below).

569

570 **Headcast Construction**

571 From an MRI-extracted image of the skull, a headcast that fit between the participant's scalp and the
572 MEG dewar was constructed (Meyer et al., 2017; Troebinger et al., 2014a). Scalp surfaces were first
573 extracted from the T1-weighted MRI scans acquired in the first MRI protocol using standard SPM12
574 procedures (<http://www.fil.ion.ucl.ac.uk/spm/>). Next, this tessellated surface was converted into the
575 standard template library (STL) format, commonly used for 3D printing. Importantly, this conversion
576 imposed only a rigid body transformation, meaning that it was easily reverse-transformable at any
577 point in space back into native MRI space. Accordingly, when the fiducial locations were optimized
578 and specified in STL space as coil-shaped protrusions on the scalp, their exact locations could be
579 retrieved and employed for co-registration. Next, the headcast design was optimized by accounting
580 for factors such as head-cast coverage in front of the ears, or angle of the bridge of the nose. To
581 specify the shape of the fiducial coils, a single coil was 3D scanned and three virtual copies of it were
582 placed at the approximate nasion, left peri-auricular (LPA), and right peri-auricular (RPA) sites, with
583 the constraint that coil placements had to have the coil-body and wire flush against the scalp, in

584 order to prevent movement of the coil when the head-cast was worn. The virtual 3D model was
585 placed inside a virtual version of the scanner dewar such that the distance to the sensors was
586 minimized (by placing the head as far up within the dewar as possible) while ensuring that vision was
587 not obstructed. Next, the head-model (plus spacing elements and coil protrusions) was printed using
588 a Zcorp 3D printer (Zprinter 510) with 600 x 540 dots per inch resolution. The 3D printed head model
589 was then placed inside the manufacturer-provided replica of the dewar and liquid resin was poured
590 in between the surfaces to fill the negative space, resulting in the subject-specific headcast. The
591 fiducial coil protrusions in the 3D model now become indentations in the resulting headcast, in
592 which the fiducial coils can sit during scanning. The anatomical landmarks used for determining the
593 spatial relationship between the brain and MEG sensors are thus in the same location for repeated
594 scans, allowing data from multiple sessions to be combined (Meyer et al., 2017).

595

596 **FreeSurfer Surface Extraction**

597 FreeSurfer (v5.3.0; Fischl, 2012) was used to extract cortical surfaces from the multi-parameter
598 maps. Use of multi-parameter maps as input to FreeSurfer can lead to localized tissue segmentation
599 failures due to boundaries between the pial surface, dura matter and CSF showing different contrast
600 compared to that assumed within FreeSurfer algorithms (Lutti et al., 2014). Therefore, an in-house
601 FreeSurfer surface reconstruction procedure was used to overcome these issues, using the PD and
602 T1 maps as inputs. Detailed methods for cortical surface reconstruction can be found in Carey et al.
603 (Carey et al., 2017). This process yields surface extractions for the pial surface (the most superficial
604 layer of the cortex adjacent to the cerebro-spinal fluid, CSF), and the white/grey matter boundary
605 (the deepest cortical layer). Each of these surfaces is downsampled by a factor of 10, resulting in two
606 meshes comprising about 30,000 vertices each ($M=30,094.75$, $SD=2,665.45$ over participants). For
607 the purpose of this paper, we will use these two surfaces to represent deep (white/grey interface)
608 and superficial (grey-CSF interface) cortical models.

609

610 **MEG Acquisition**

611 MEG recordings were made using a 275-channel Canadian Thin Films (CTF) MEG system with
612 superconducting quantum interference device (SQUID)-based axial gradiometers (VSM MedTech,
613 Vancouver, Canada) in a magnetically shielded room. The data collected were digitized continuously
614 at a sampling rate of 1200 Hz. A projector displayed the visual stimuli on a screen (~8m from the
615 participant), and participants made responses with a button box.

616

617 **Behavioral Analyses**

618 Participant responses were classified as correct when the button pressed matched the direction of
619 the instruction cue, and incorrect otherwise. The response time (RT) was measured as the time of
620 button press relative to the onset of the instruction cue. Both measures were analyzed using
621 repeated measures ANOVAs with congruence (congruent or incongruent) and coherence (low,
622 medium, and high) as factors. Pairwise follow-up tests were performed between congruence levels
623 at each coherence level, Bonferroni corrected.

624

625 **MEG Preprocessing**

626 All MEG data preprocessing and analyses were performed using SPM12
627 (<http://www.fil.ion.ucl.ac.uk/spm/>) using Matlab R2014a and are available at
628 <http://github.com/jbonaiuto/meg-laminar>. The data were filtered (5th order butterworth bandpass
629 filter: 2-100 Hz) and downsampled to 250 Hz. Eye-blink artifacts were removed using multiple source
630 eye correction (Berg and Scherg, 1994). Trials were then epoched from 1s before RDK onset to 1.5s
631 after instruction cue onset, and from 2s before the participant's response to 2s after. Blocks within
632 each session were merged, and trials whose variance exceeded 2.5 standard deviations from the
633 mean were excluded from analysis.

634

635 **Source reconstruction**

636 Source inversion was performed using the empirical Bayesian beamformer (EBB; Belardinelli et al.,
637 2012; López et al., 2014) within SPM. The sensor data were first reduced into 180 orthogonal spatial
638 (lead field) modes and 16 temporal modes. The empirical Bayes optimization rests upon estimating
639 hyper-parameters which express the relative contribution of source and sensor level covariance
640 priors to the data (López et al., 2014). We assumed the sensor level covariance to be an identity
641 matrix, with a single source level prior estimated from the data. The source level prior was based on
642 the beamformer power estimate across a two-layer manifold comprised of pial and white cortical
643 surfaces with source orientations defined as normal to the cortical surface. There were therefore
644 only two hyper-parameters to estimate – defining the relative contribution of the source and sensor
645 level covariance components to the data. We used the Nolte single shell head model as
646 implemented in SPM (Nolte, 2003).

647

648 **Analyses for Laminar Discrimination**

649 The laminar analysis reconstructed the data onto a mesh combining the pial and white matter
650 surfaces, thus providing an estimate of source activity on both surfaces (**Figure 3**). We analyzed six
651 different visual and sensorimotor signals at different frequencies and time windows of interest
652 (WOIs): RDK-aligned visual alpha (7-13Hz; WOI=[0s, 2s]; baseline WOI=[-1s, -.5s]), RDK-aligned visual
653 gamma (60-90Hz; WOI=[250ms, 500ms]; baseline WOI=[-500ms, -250ms]), instruction cue-aligned
654 visual gamma (60-90Hz; WOI=[100ms, 500ms]; baseline WOI=[-500ms, -100ms]), RDK-aligned
655 sensorimotor beta (15-30Hz; WOI=[0s, 2s]; baseline WOI=[-500ms, 0ms]), response-aligned
656 sensorimotor beta (15-30Hz; WOI=[500ms, 1s]; baseline WOI=[-250ms 250ms]), response-aligned
657 sensorimotor gamma (60-90Hz; WOI=[-100ms, 200ms]; baseline WOI=[-1.5s, -1s]). For each signal,
658 we defined an ROI by comparing power in the associated frequency band during the WOI with a
659 prior baseline WOI at each vertex and averaging over trials. Vertices in either surface with a mean
660 value in the 80th percentile over all vertices in that surface, as well as the corresponding vertices in
661 the other surface, were included in the ROI. This ensured that the contrast used to define the ROI
662 was orthogonal to the subsequent pial versus white matter surface contrast. For each trial, ROI
663 values for the pial and white matter surfaces were computed by averaging the absolute value of the
664 change in power compared to baseline in that surface within the ROI. Finally, a paired t-test was
665 used to compare the ROI values from the pial surface with those from the white matter surface over
666 trials (**Figure 3**). This resulted in positive t-statistics when the change in power was greatest on the
667 pial surface, and negative values when the change was greatest on the white matter surface. All t-
668 tests were performed with corrected noise variance estimates in order to attenuate artifactually
669 high significance values (Ridgway et al., 2012).

670 The control analyses utilized the same procedure, but each introduced some perturbation to the
671 data. The shuffled analysis permuted the lead fields of the forward model prior to source
672 reconstruction in order to destroy any correspondence between the cortical surface geometry and
673 the sensor data. This was repeated 10 times per session, with a different random lead field
674 permutation each time. Each permutation was then used in the laminar analysis for every low and
675 high frequency signal. The co-registration error analysis introduced a rotation ($M=10^\circ$, $SD=2.5^\circ$) and
676 translation ($M=10\text{mm}$, $SD=2.5\text{mm}$) in a random direction of the fiducial coil locations prior to source
677 inversion, simulating between-session co-registration error. This was done 10 times per session, with
678 a different random rotation and translation each time. Again, each perturbation was used in the
679 laminar analysis for every low and high frequency signal. The SNR analysis used a random subset of
680 the available trials from each subject, gradually increasing the number of trials used from 10 to the
681 number of trials available. This was repeated 10 times, using a different random subset of trials each
682 time, and the resulting t-statistics were averaged.

683

684 **Condition Comparison**

685 For each visual and sensorimotor frequency band/task epoch combination, induced activity was
686 compared between task conditions on the surface and within the anatomically constrained ROI
687 identified from the corresponding laminar analysis. Seven-cycle Morlet wavelets were used to
688 compute power within the frequency band and this was baseline-corrected in a frequency-specific
689 manner using robust averaging. For each participant, the mean percent change in power over the
690 WOI was averaged over all trials within every condition. Wilcoxon tests for comparing two repeated
691 measures were used to compare the change in power for instruction cue-aligned visual gamma and
692 sensorimotor beta rebound between congruent and incongruent trials. A Friedman test for
693 comparing multiple levels of a single factor with repeated measures was used to compare the
694 sensorimotor beta decrease between low, medium, and high RDK coherence trials. This was
695 followed up by Tukey-Kramer corrected pairwise comparisons. Only trials in which a correct
696 response was made were analyzed.

697

698 **Author contributions**

699 Conceptualization, J.J.B., G.R.B., and S.B.; Methodology, J.J.B., S.S.M., M.F.C., F.D., G.R.B., and S.B.;
700 Formal Analysis, J.J.B.; Investigation, J.J.B. and S.S.M., Writing – Original Draft, J.J.B., S.S.M., S.L.,
701 H.R., M.F.C., F.D., G.R.B., and S.B.; Writing – Review and Editing, J.J.B., S.S.M., S.L., H.R., M.F.C., F.D.,
702 G.R.B., and S.B.; Supervision, S.B. and G.R.B.; Funding Acquisition, S.B, GRB.

703

704 **Acknowledgements**

705 JB is funded by a BBSRC research grant (BB/M009645/1). SM is supported by a Medical Research
706 Council and Engineering and Physical Sciences Research Council grant MR/K6010/86010/1, the
707 Medical Research Council UKMEG Partnership grant MR/K005464/1, and a Wellcome Principal
708 Research Fellowship to Neil Burgess. SL is supported by a Wellcome Trust clinical postdoctoral grant
709 (105804/Z/14/Z). The WCHN is supported by a strategic award from Wellcome (091593/Z/10/Z).

710

711 **References**

- 712 Adams, R.A., Shipp, S., and Friston, K.J. (2013). Predictions not commands: active inference in the
713 motor system. *Brain Struct. Funct.* *218*, 611–643.
- 714 Arnal, L.H., and Giraud, A.-L. (2012). Cortical oscillations and sensory predictions. *Trends Cogn. Sci.*
715 *16*, 390–398.
- 716 Arnal, L.H., Wyart, V., and Giraud, A.-L. (2011). Transitions in neural oscillations reflect prediction
717 errors generated in audiovisual speech. *Nat. Neurosci.* *14*, 797–801.
- 718 Baillet, S. (2017). Magnetoencephalography for brain electrophysiology and imaging. *Nat. Neurosci.*
719 *20*, 327–339.
- 720 Barbas, H., and Pandya, D.N. (1989). Architecture and intrinsic connections of the prefrontal cortex
721 in the rhesus monkey. *J. Comp. Neurol.* *286*, 353–375.
- 722 Barone, P., Batardiere, A., Knoblauch, K., and Kennedy, H. (2000). Laminar distribution of neurons in
723 extrastriate areas projecting to visual areas V1 and V4 correlates with the hierarchical rank and
724 indicates the operation of a distance rule. *J. Neurosci.* *20*, 3263–3281.
- 725 Bastos, A.M., Usrey, W.M., Adams, R.A., Mangun, G.R., Fries, P., and Friston, K.J. (2012). Canonical
726 microcircuits for predictive coding. *Neuron* *76*, 695–711.
- 727 Belardinelli, P., Ortiz, E., Barnes, G., Noppeney, U., and Preissl, H. (2012). Source reconstruction
728 accuracy of MEG and EEG Bayesian inversion approaches. *PLoS One* *7*, e51985.
- 729 Berg, P., and Scherg, M. (1994). A multiple source approach to the correction of eye artifacts.
730 *Electroencephalogr. Clin. Neurophysiol.* *90*, 229–241.
- 731 Bollimunta, A., Chen, Y., Schroeder, C.E., and Ding, M. (2008). Neuronal Mechanisms of Cortical
732 Alpha Oscillations in Awake-Behaving Macaques. *J. Neurosci.* *28*.
- 733 Bollimunta, A., Mo, J., Schroeder, C.E., and Ding, M. (2011). Neuronal mechanisms and attentional
734 modulation of corticothalamic α oscillations. *J. Neurosci. Off. J. Soc. Neurosci.* *31*, 4935–4943.

- 735 Bonaiuto, J.J., Rossiter, H.E., Meyer, S.S., Adams, N., Little, S., Callaghan, M.F., Dick, F., Bestmann, S.,
736 and Barnes, G.R. (2017). Non-invasive laminar inference with MEG: Comparison of methods and
737 source inversion algorithms. *bioRxiv*.
- 738 Buffalo, E.A., Fries, P., Landman, R., Buschman, T.J., and Desimone, R. (2011). Laminar differences in
739 gamma and alpha coherence in the ventral stream. *Proc. Natl. Acad. Sci. U. S. A.* *108*, 11262–11267.
- 740 Busch, N.A., Debener, S., Kranczioch, C., Engel, A.K., and Herrmann, C.S. (2004). Size matters: effects
741 of stimulus size, duration and eccentricity on the visual gamma-band response. *Clin. Neurophysiol.*
742 *115*, 1810–1820.
- 743 Buzsáki, G., and Wang, X.-J. (2012). Mechanisms of gamma oscillations. *Annu. Rev. Neurosci.* *35*,
744 203–225.
- 745 Callaghan, M.F., Josephs, O., Herbst, M., Zaitsev, M., Todd, N., and Weiskopf, N. (2015). An
746 evaluation of prospective motion correction (PMC) for high resolution quantitative MRI. *Front.*
747 *Neurosci.* *9*, 97.
- 748 Cardin, J.A., Carlén, M., Meletis, K., Knoblich, U., Zhang, F., Deisseroth, K., Tsai, L.-H., and Moore, C.I.
749 (2009). Driving fast-spiking cells induces gamma rhythm and controls sensory responses. *Nature* *459*,
750 663–667.
- 751 Carey, D., Caprini, F., Allen, M., Lutti, A., Weiskopf, N., Rees, G., Callaghan, M.F., and Dick, F. (2017).
752 Quantitative MRI Provides Markers Of Intra-, Inter-Regional, And Age-Related Differences In Young
753 Adult Cortical Microstructure. *bioRxiv*.
- 754 Carlén, M., Meletis, K., Siegle, J.H., Cardin, J.A., Futai, K., Vierling-Claassen, D., Rühlmann, C., Jones,
755 S.R., Deisseroth, K., Sheng, M., et al. (2012). A critical role for NMDA receptors in parvalbumin
756 interneurons for gamma rhythm induction and behavior. *Mol. Psychiatry* *17*, 537–548.
- 757 Cassim, F., Monaca, C., Szurhaj, W., Bourriez, J.L., Defebvre, L., Derambure, P., and Guieu, J.D.
758 (2001). Does post-movement beta synchronization reflect an idling motor cortex? *Neuroreport* *12*,
759 3859–3863.
- 760 Cheyne, D., and Ferrari, P. (2013). MEG studies of motor cortex gamma oscillations: evidence for a
761 gamma “fingerprint” in the brain? *Front. Hum. Neurosci.* *7*, 575.
- 762 Cheyne, D., Bells, S., Ferrari, P., Gaetz, W., and Bostan, A.C. (2008). Self-paced movements induce
763 high-frequency gamma oscillations in primary motor cortex. *Neuroimage* *42*, 332–342.
- 764 Cohen, M.X. (2017). Where Does EEG Come From and What Does It Mean? *Trends Neurosci.* *40*,
765 208–218.
- 766 Crone, N., Miglioretti, D.L., Gordon, B., and Lesser, R.P. (1998). Functional mapping of human
767 sensorimotor cortex with electrocorticographic spectral analysis. II. Event-related synchronization in
768 the gamma band. *Brain* *121*, 2301–2315.
- 769 Curtis, C.E., and Lee, D. (2010). Beyond working memory: the role of persistent activity in decision
770 making. *Trends Cogn. Sci.* *14*, 216–222.
- 771 Donner, T.H., and Siegel, M. (2011). A framework for local cortical oscillation patterns. *Trends Cogn.*
772 *Sci.* *15*, 191–199.
- 773 Donner, T.H., Siegel, M., Fries, P., and Engel, A.K. (2009). Buildup of choice-predictive activity in
774 human motor cortex during perceptual decision making. *Curr. Biol.* *19*, 1581–1585.
- 775 Engel, A.K., and Fries, P. (2010). Beta-band oscillations--signalling the status quo? *Curr. Opin.*
776 *Neurobiol.* *20*, 156–165.
- 777 Felleman, D.J., and Van Essen, D.C. (1991). Distributed hierarchical processing in the primate
778 cerebral cortex. *Cereb Cortex* *1*, 1–47.
- 779 Fischl, B. (2012). FreeSurfer. *Neuroimage* *62*, 774–781.
- 780 Fischl, B., and Dale, A.M. (2000). Measuring the thickness of the human cerebral cortex from
781 magnetic resonance images. *Proc. Natl. Acad. Sci. U. S. A.* *97*, 11050–11055.
- 782 Fontolan, L., Morillon, B., Liegeois-Chauvel, C., and Giraud, A.-L. (2014). The contribution of
783 frequency-specific activity to hierarchical information processing in the human auditory cortex. *Nat.*
784 *Commun.* *5*, 4694.

- 785 Fries, P. (2005). A mechanism for cognitive dynamics: neuronal communication through neuronal
786 coherence. *Trends Cogn. Sci.* 9, 474–480.
- 787 Fries, P. (2015). Rhythms for Cognition: Communication through Coherence. *Neuron* 88, 220–235.
- 788 Fries, P., Reynolds, J., Rorie, A.E., and Desimone, R. (2001). Modulation of Oscillatory Neuronal
789 Synchronization by Selective Visual Attention. *Science* (80-.). 291, 1560–1563.
- 790 Friston, K., and Kiebel, S. (2009). Predictive coding under the free-energy principle. *Philos. Trans. R.*
791 *Soc. Lond. B. Biol. Sci.* 364, 1211–1221.
- 792 Gaetz, W., Edgar, J.C., Wang, D.J., and Roberts, T.P.L. (2011). Relating MEG measured motor cortical
793 oscillations to resting γ -Aminobutyric acid (GABA) concentration. *Neuroimage* 55, 616–621.
- 794 Georgiev, D., Rocchi, L., Tocco, P., Speekenbrink, M., Rothwell, J.C., and Jahanshahi, M. (2016).
795 Continuous Theta Burst Stimulation Over the Dorsolateral Prefrontal Cortex and the Pre-SMA Alter
796 Drift Rate and Response Thresholds Respectively During Perceptual Decision-Making. *Brain Stimul.* 9,
797 601–608.
- 798 Griswold, M.A., Jakob, P.M., Heidemann, R.M., Nittka, M., Jellus, V., Wang, J., Kiefer, B., and Haase,
799 A. (2002). Generalized autocalibrating partially parallel acquisitions (GRAPPA). *Magn. Reson. Med.*
800 47, 1202–1210.
- 801 Gurtubay, I.G., Alegre, M., Labarga, A., Malanda, A., Iriarte, J., and Artieda, J. (2001). Gamma band
802 activity in an auditory oddball paradigm studied with the wavelet transform. *Clin. Neurophysiol.* 112,
803 1219–1228.
- 804 Haegens, S., Nácher, V., Hernández, A., Luna, R., Jensen, O., and Romo, R. (2011). Beta oscillations in
805 the monkey sensorimotor network reflect somatosensory decision making. *Proc. Natl. Acad. Sci. U.*
806 *S. A.* 108, 10708–10713.
- 807 Haegens, S., Barczak, A., Musacchia, G., Lipton, M.L., Mehta, A.D., Lakatos, P., and Schroeder, C.E.
808 (2015). Laminar Profile and Physiology of the Rhythm in Primary Visual, Auditory, and
809 Somatosensory Regions of Neocortex. *J. Neurosci.* 35, 14341–14352.
- 810 Hanks, T.D., Ditterich, J., and Shadlen, M.N. (2006). Microstimulation of macaque area LIP affects
811 decision-making in a motion discrimination task. *Nat. Neurosci.* 9, 682–689.
- 812 Hari, R., and Salmelin, R. (1997). Human cortical oscillations: A neuromagnetic view through the
813 skull. *Trends Neurosci.* 20, 44–49.
- 814 Heekeren, H., Marrett, S., Ruff, D.A., Bandettini, P., and Ungerleider, L.G. (2006). Involvement of
815 human left dorsolateral prefrontal cortex in perceptual decision making is independent of response
816 modality. *Proc. Natl. Acad. Sci. U. S. A.* 103, 10023–10028.
- 817 Heekeren, H.R., Marrett, S., Bandettini, P.A., and Ungerleider, L.G. (2004). A general mechanism for
818 perceptual decision-making in the human brain. *Nature* 431, 859–862.
- 819 Hilgetag, C.C., and Barbas, H. (2006). Role of Mechanical Factors in the Morphology of the Primate
820 Cerebral Cortex. *PLoS Comput. Biol.* 2, e22.
- 821 Hillebrand, A., and Barnes, G.R. (2002). A quantitative assessment of the sensitivity of whole-head
822 MEG to activity in the adult human cortex. *Neuroimage* 16, 638–650.
- 823 Hillebrand, A., and Barnes, G.R. (2003). The use of anatomical constraints with MEG beamformers.
824 *Neuroimage* 20, 2302–2313.
- 825 Hillebrand, A., and Barnes, G.R. (2011). Practical constraints on estimation of source extent with
826 MEG beamformers. *Neuroimage* 54, 2732–2740.
- 827 Hoogenboom, N., Schoffelen, J.-M., Oostenveld, R., Parkes, L.M., and Fries, P. (2006). Localizing
828 human visual gamma-band activity in frequency, time and space. *Neuroimage* 29, 764–773.
- 829 Huo, X., Xiang, J., Wang, Y., Kirtman, E.G., Kotecha, R., Fujiwara, H., Hemasilpin, N., Rose, D.F., and
830 Degrauw, T. (2010). Gamma oscillations in the primary motor cortex studied with MEG. *Brain Dev.*
831 32, 619–624.
- 832 Hussar, C.R., and Pasternak, T. (2013). Common rules guide comparisons of speed and direction of
833 motion in the dorsolateral prefrontal cortex. *J. Neurosci.* 33, 972–986.
- 834 Jensen, O., and Mazaheri, A. (2010). Shaping Functional Architecture by Oscillatory Alpha Activity:
835 Gating by Inhibition. *Front. Hum. Neurosci.* 4, 186.

- 836 Jensen, O., Bonnefond, M., Marshall, T.R., and Tiesinga, P. (2015). Oscillatory mechanisms of
837 feedforward and feedback visual processing. *Trends Neurosci.* *38*, 192–194.
- 838 Jones, S.R. (2016). When brain rhythms aren't "rhythmic": implication for their mechanisms and
839 meaning. *Curr. Opin. Neurobiol.* *40*, 72–80.
- 840 Jones, S.E., Buchbinder, B.R., and Aharon, I. (2000). Three-dimensional mapping of cortical thickness
841 using Laplace's equation. *Hum. Brain Mapp.* *11*, 12–32.
- 842 Jurkiewicz, M.T., Gaetz, W.C., Bostan, A.C., and Cheyne, D. (2006). Post-movement beta rebound is
843 generated in motor cortex: Evidence from neuromagnetic recordings. *Neuroimage* *32*, 1281–1289.
- 844 Kabani, N., Le Goualher, G., MacDonald, D., and Evans, A.C. (2001). Measurement of Cortical
845 Thickness Using an Automated 3-D Algorithm: A Validation Study. *Neuroimage* *13*, 375–380.
- 846 Kayser, A.S., Buchsbaum, B.R., Erickson, D.T., and D'Esposito, M. (2010). The Functional Anatomy of
847 a Perceptual Decision in the Human Brain. *J. Neurophysiol.* *103*, 1179–1194.
- 848 Van Kerkoerle, T., Self, M.W., Dagnino, B., Gariel-Mathis, M.-A., Poort, J., van der Togt, C., and
849 Roelfsema, P.R. (2014). Alpha and gamma oscillations characterize feedback and feedforward
850 processing in monkey visual cortex. *Proc. Natl. Acad. Sci. U. S. A.* *111*, 14332–14341.
- 851 Kok, P., Bains, L.J., van Mourik, T., Norris, D.G., and de Lange, F.P. (2016). Selective Activation of the
852 Deep Layers of the Human Primary Visual Cortex by Top-Down Feedback. *Curr. Biol.* *26*, 371–376.
- 853 Koopmans, P.J., Barth, M., and Norris, D.G. (2010). Layer-specific BOLD activation in human V1. *Hum.*
854 *Brain Mapp.* *31*, 1297–1304.
- 855 De Lange, F.P., Rahnev, D.A., Donner, T.H., and Lau, H. (2013). Prestimulus oscillatory activity over
856 motor cortex reflects perceptual expectations. *J. Neurosci.* *33*, 1400–1410.
- 857 Larson, E., Maddox, R.K., and Lee, A.K.C. (2014). Improving spatial localization in MEG inverse
858 imaging by leveraging intersubject anatomical differences. *Front. Neurosci.* *8*, 330.
- 859 Lee, S., and Jones, S.R. (2013). Distinguishing mechanisms of gamma frequency oscillations in human
860 current source signals using a computational model of a laminar neocortical network. *Front. Hum.*
861 *Neurosci.* *7*, 869.
- 862 Lee, J.H., Whittington, M.A., Kopell, N.J., Deuchars, J., and Silberberg, G. (2013). Top-Down Beta
863 Rhythms Support Selective Attention via Interlaminar Interaction: A Model. *PLoS Comput. Biol.* *9*,
864 e1003164.
- 865 Lerch, J.P., and Evans, A.C. (2005). Cortical thickness analysis examined through power analysis and a
866 population simulation. *Neuroimage* *24*, 163–173.
- 867 López, J.D., Litvak, V., Espinosa, J.J., Friston, K., and Barnes, G.R. (2014). Algorithmic procedures for
868 Bayesian MEG/EEG source reconstruction in SPM. *Neuroimage* *84*, 476–487.
- 869 Lutti, A., Hutton, C., Finsterbusch, J., Helms, G., and Weiskopf, N. (2010). Optimization and validation
870 of methods for mapping of the radiofrequency transmit field at 3T. *Magn. Reson. Med.* *64*, 229–238.
- 871 Lutti, A., Stadler, J., Josephs, O., Windischberger, C., Speck, O., Bernarding, J., Hutton, C., and
872 Weiskopf, N. (2012). Robust and fast whole brain mapping of the RF transmit field B1 at 7T. *PLoS*
873 *One* *7*, e32379.
- 874 Lutti, A., Dick, F., Sereno, M.I., and Weiskopf, N. (2014). Using high-resolution quantitative mapping
875 of R1 as an index of cortical myelination. *Neuroimage* *93*, 176–188.
- 876 MacDonald, D., Kabani, N., Avis, D., and Evans, A.C. (2000). Automated 3-D Extraction of Inner and
877 Outer Surfaces of Cerebral Cortex from MRI. *Neuroimage* *12*, 340–356.
- 878 Maier, A., Adams, G.K., Aura, C., and Leopold, D.A. (2010). Distinct Superficial and deep laminar
879 domains of activity in the visual cortex during rest and stimulation. *Front. Syst. Neurosci.* *4*.
- 880 Markov, N.T., Ercsey-Ravasz, M., Van Essen, D.C., Knoblauch, K., Toroczkai, Z., and Kennedy, H.
881 (2013). Cortical high-density counterstream architectures. *Science* *342*, 1238406.
- 882 Markov, N.T., Ercsey-Ravasz, M.M., Ribeiro Gomes, A.R., Lamy, C., Magrou, L., Vezoli, J., Misery, P.,
883 Falchier, A., Quilodran, R., Gariel, M.A., et al. (2014a). A Weighted and Directed Interareal
884 Connectivity Matrix for Macaque Cerebral Cortex. *Cereb. Cortex* *24*, 17–36.

- 885 Markov, N.T., Vezoli, J., Chameau, P., Falchier, A., Quilodran, R., Huissoud, C., Lamy, C., Misery, P.,
886 Giroud, P., Ullman, S., et al. (2014b). Anatomy of hierarchy: Feedforward and feedback pathways in
887 macaque visual cortex. *J. Comp. Neurol.* *522*, 225–259.
- 888 Matelli, M., Luppino, G., and Rizzolatti, G. (1991). Architecture of superior and mesial area 6 and the
889 adjacent cingulate cortex in the macaque monkey. *J Comp Neurol* *311*, 445–462.
- 890 Mazaheri, A., van Schouwenburg, M.R., Dimitrijevic, A., Denys, D., Cools, R., and Jensen, O. (2014).
891 Region-specific modulations in oscillatory alpha activity serve to facilitate processing in the visual
892 and auditory modalities. *Neuroimage* *87*, 356–362.
- 893 Medvedovsky, M., Taulu, S., Bikmullina, R., and Paetau, R. (2007). Artifact and head movement
894 compensation in MEG. *Neurol. Neurophysiol. Neurosci.* *4*.
- 895 Mehrkanoon, S., Breakspear, M., and Boonstra, T.W. (2014). The reorganization of corticomuscular
896 coherence during a transition between sensorimotor states. *Neuroimage* *100*, 692–702.
- 897 Mejias, J.F., Murray, J.D., Kennedy, H., and Wang, X.-J. (2016). Feedforward and feedback frequency-
898 dependent interactions in a large-scale laminar network of the primate cortex. *Sci Adv* *2*, e1601335.
- 899 Meyer, S.S., Bonaiuto, J., Lim, M., Rossiter, H., Waters, S., Bradbury, D., Bestmann, S., Brookes, M.,
900 Callaghan, M.F., Weiskopf, N., et al. (2017). Flexible head-casts for high spatial precision MEG. *J.*
901 *Neurosci. Methods* *276*, 38–45.
- 902 Michalareas, G., Vezoli, J., van Pelt, S., Schoffelen, J.-M., Kennedy, H., and Fries, P. (2016). Alpha-
903 Beta and Gamma Rhythms Subserve Feedback and Feedforward Influences among Human Visual
904 Cortical Areas. *Neuron* *89*, 384–397.
- 905 Müller, M.M., Bosch, J., Elbert, T., Kreiter, A., Sosa, M. V, Sosa, P. V, and Rockstroh, B. (1996).
906 Visually induced gamma-band responses in human electroencephalographic activity--a link to animal
907 studies. *Exp. Brain Res.* *112*, 96–102.
- 908 Muthukumaraswamy, S.D. (2010). Functional Properties of Human Primary Motor Cortex Gamma
909 Oscillations. *J. Neurophysiol.* *104*, 2873–2885.
- 910 Muthukumaraswamy, S.D., and Singh, K.D. (2013). Visual gamma oscillations: The effects of stimulus
911 type, visual field coverage and stimulus motion on MEG and EEG recordings. *Neuroimage* *69*, 223–
912 230.
- 913 Nandy, A.S., Nassi, J.J., and Reynolds, J.H. (2017). Laminar Organization of Attentional Modulation in
914 Macaque Visual Area V4. *Neuron* *93*, 235–246.
- 915 Nolte, G. (2003). The magnetic lead field theorem in the quasi-static approximation and its use for
916 magnetoencephalography forward calculation in realistic volume conductors. *Phys. Med. Biol.* *48*,
917 3637–3652.
- 918 Olman, C.A., Harel, N., Feinberg, D.A., He, S., Zhang, P., Ugurbil, K., and Yacoub, E. (2012). Layer-
919 Specific fMRI Reflects Different Neuronal Computations at Different Depths in Human V1. *PLoS One*
920 *7*, e32536.
- 921 Parkes, L.M., Bastiaansen, M.C.M., and Norris, D.G. (2006). Combining EEG and fMRI to investigate
922 the post-movement beta rebound. *Neuroimage* *29*, 685–696.
- 923 Pfurtscheller, G., and Neuper, C. (1997). Motor imagery activates primary sensorimotor area in
924 humans. *Neurosci. Lett.* *239*, 65–68.
- 925 Pfurtscheller, G., Stancák, A., and Neuper, C. (1996). Post-movement beta synchronization. A
926 correlate of an idling motor area? *Electroencephalogr. Clin. Neurophysiol.* *98*, 281–293.
- 927 Pinotsis, D.A., Geerts, J.P., Pinto, L., FitzGerald, T.H.B., Litvak, V., Auksztulewicz, R., and Friston, K.J.
928 (2017). Linking canonical microcircuits and neuronal activity: Dynamic causal modelling of laminar
929 recordings. *Neuroimage* *146*, 355–366.
- 930 Platt, M.L., and Glimcher, P.W. (1999). Neural correlates of decision variables in parietal cortex.
931 *Nature* *400*, 233–238.
- 932 Rajkowska, G., and Goldman-Rakic, P.S. (1995). Cytoarchitectonic Definition of Prefrontal Areas in
933 the Normal Human Cortex: I. Remapping of Areas 9 and 46 using Quantitative Criteria. *Cereb. Cortex*
934 *5*, 307–322.

- 935 Roopun, A.K., Middleton, S.J., Cunningham, M.O., LeBeau, F.E.N., Bibbig, A., Whittington, M.A., and
936 Traub, R.D. (2006). A beta2-frequency (20-30 Hz) oscillation in nonsynaptic networks of
937 somatosensory cortex. *Proc. Natl. Acad. Sci. U. S. A.* *103*, 15646–15650.
- 938 Roopun, A.K., Lebeau, F.E.N., Rammell, J., Cunningham, M.O., Traub, R.D., and Whittington, M.A.
939 (2010). Cholinergic neuromodulation controls directed temporal communication in neocortex in
940 vitro. *Front. Neural Circuits* *4*, 8.
- 941 Sajad, A., Godlove, D.C., and Schall, J.D. (2017). Microcircuitry of Performance Monitoring. *bioRxiv*.
- 942 Salmelin, R., Hämäläinen, M., Kajola, M., and Hari, R. (1995). Functional segregation of movement-
943 related rhythmic activity in the human brain. *Neuroimage* *2*, 237–243.
- 944 Sauseng, P., Klimesch, W., Stadler, W., Schabus, M., Doppelmayr, M., Hanslmayr, S., Gruber, W.R.,
945 and Birbaumer, N. (2005). A shift of visual spatial attention is selectively associated with human EEG
946 alpha activity. *Eur. J. Neurosci.* *22*, 2917–2926.
- 947 Scheeringa, R., and Fries, P. (2017). Cortical layers, rhythms and BOLD signals. *Neuroimage*.
- 948 Sherman, M.A., Lee, S., Law, R., Haegens, S., Thorn, C.A., Hämäläinen, M.S., Moore, C.I., and Jones,
949 S.R. (2016). Neural mechanisms of transient neocortical beta rhythms: Converging evidence from
950 humans, computational modeling, monkeys, and mice. *Proc. Natl. Acad. Sci. U. S. A.* *113*, E4885–
951 E4894.
- 952 Smith, M.A., Jia, X., Zandvakili, A., and Kohn, A. (2013). Laminar dependence of neuronal correlations
953 in visual cortex. *J. Neurophysiol.* *109*, 940–947.
- 954 Sohal, V.S., Zhang, F., Yizhar, O., and Deisseroth, K. (2009). Parvalbumin neurons and gamma
955 rhythms enhance cortical circuit performance. *Nature* *459*, 698–702.
- 956 Sotero, R.C., Bortel, A., Naaman, S., Mocanu, V.M., Kropf, P., Villeneuve, M.Y., and Shmuel, A. (2015).
957 Laminar Distribution of Phase-Amplitude Coupling of Spontaneous Current Sources and Sinks. *Front.*
958 *Neurosci.* *9*, 454.
- 959 Spaak, E., Bonnefond, M., Maier, A., Leopold, D.A., and Jensen, O. (2012). Layer-specific entrainment
960 of γ -band neural activity by the α rhythm in monkey visual cortex. *Curr. Biol. CB* *22*, 2313–2318.
- 961 Stephan, K.E., Petzschner, F.H., Kasper, L., Bayer, J., Wellstein, K.V., Stefanics, G., Pruessmann, K.P.,
962 and Heinzle, J. (2017). Laminar fMRI and computational theories of brain function. *Neuroimage*.
- 963 Sun, W., and Dan, Y. (2009). Layer-specific network oscillation and spatiotemporal receptive field in
964 the visual cortex. *Proc. Natl. Acad. Sci. U. S. A.* *106*, 17986–17991.
- 965 Tan, H., Jenkinson, N., and Brown, P. (2014). Dynamic Neural Correlates of Motor Error Monitoring
966 and Adaptation during Trial-to-Trial Learning. *J. Neurosci.* *34*, 5678–5688.
- 967 Tan, H., Wade, C., and Brown, P. (2016). Post-Movement Beta Activity in Sensorimotor Cortex
968 Indexes Confidence in the Estimations from Internal Models. *J. Neurosci.* *36*, 1516–1528.
- 969 Thut, G. (2006). β -Band Electroencephalographic Activity over Occipital Cortex Indexes Visuospatial
970 Attention Bias and Predicts Visual Target Detection. *J. Neurosci.* *26*, 9494–9502.
- 971 Tiesinga, P., and Sejnowski, T.J. (2009). Cortical Enlightenment: Are Attentional Gamma Oscillations
972 Driven by ING or PING? *Neuron* *63*, 727–732.
- 973 Todorovic, A., van Ede, F., Maris, E., and de Lange, F.P. (2011). Prior Expectation Mediates Neural
974 Adaptation to Repeated Sounds in the Auditory Cortex: An MEG Study. *J. Neurosci.* *31*, 9118–9123.
- 975 Torrecillos, F., Alayrangues, J., Kilavik, B.E., and Malfait, N. (2015). Distinct Modulations in
976 Sensorimotor Postmovement and Foreperiod β -Band Activities Related to Error Salience Processing
977 and Sensorimotor Adaptation. *J. Neurosci.* *35*, 12753–12765.
- 978 Tosoni, A., Galati, G., Romani, G.L., and Corbetta, M. (2008). Sensory-motor mechanisms in human
979 parietal cortex underlie arbitrary visual decisions. *Nat. Neurosci.* *11*, 1446–1453.
- 980 Troebinger, L., López, J.D., Lutti, A., Bradbury, D., Bestmann, S., and Barnes, G. (2014a). High
981 precision anatomy for MEG. *Neuroimage* *86*, 583–591.
- 982 Troebinger, L., López, J.D., Lutti, A., Bestmann, S., and Barnes, G. (2014b). Discrimination of cortical
983 laminae using MEG. *Neuroimage* *102*, 885–893.
- 984 Uutela, K., Taulu, S., and Hämäläinen, M. (2001). Detecting and Correcting for Head Movements in
985 Neuromagnetic Measurements. *Neuroimage* *14*, 1424–1431.

- 986 Wang, X.-J. (2010). Neurophysiological and computational principles of cortical rhythms in cognition.
987 *Physiol. Rev.* *90*, 1195–1268.
- 988 Wang, P., Knösche, T.R., Rajj, T., Bonmassar, G., and Devore, S. (2013). A Realistic Neural Mass Model
989 of the Cortex with Laminar-Specific Connections and Synaptic Plasticity – Evaluation with Auditory
990 Habituation. *PLoS One* *8*, e77876.
- 991 Watson, A.B., and Pelli, D.G. (1983). Quest: A Bayesian adaptive psychometric method. *Percept.*
992 *Psychophys.* *33*, 113–120.
- 993 Weiskopf, N., Suckling, J., Williams, G., Correia, M.M., Inkster, B., Tait, R., Ooi, C., Bullmore, E.T., and
994 Lutti, A. (2013). Quantitative multi-parameter mapping of R1, PD(*), MT, and R2(*) at 3T: a multi-
995 center validation. *Front. Neurosci.* *7*, 95.
- 996 Whittington, M.A., Cunningham, M.O., LeBeau, F.E.N., Racca, C., and Traub, R.D. (2011). Multiple
997 origins of the cortical gamma rhythm. *Dev. Neurobiol.* *71*, 92–106.
- 998 Xing, D., Yeh, C.-I., Burns, S., and Shapley, R.M. (2012). Laminar analysis of visually evoked activity in
999 the primary visual cortex. *Proc. Natl. Acad. Sci. U. S. A.* *109*, 13871–13876.
- 1000 Yamagishi, N., Goda, N., Callan, D.E., Anderson, S.J., and Kawato, M. (2005). Attentional shifts
1001 towards an expected visual target alter the level of alpha-band oscillatory activity in the human
1002 calcarine cortex. *Cogn. Brain Res.* *25*, 799–809.
- 1003 Yamawaki, N., Stanford, I.M., Hall, S.D., and Woodhall, G.L. (2008). Pharmacologically induced and
1004 stimulus evoked rhythmic neuronal oscillatory activity in the primary motor cortex in vitro.
1005 *Neuroscience* *151*, 386–395.
- 1006